INL/EXT-21-64522

# Light Water Reactor Sustainability Program

# Reactor Pressure Vessel Fracture Mechanics Development and Concrete Application Testing for Grizzly

Benjamin W. Spencer
William M. Hoffman
Amit Jain
Sudipta Biswas
Somayajulu L. N. Dhulipala

September 2021

DOE Office of Nuclear Energy

# ABSTRACT

The Grizzly code is being developed to address degradation issues in nuclear reactor structures and components. For light-water reactors, Grizzly currently has capabilities to simulate degradation processes and their effects on structural integrity in two key areas: reactor pressure vessels (RPVs) and reinforced concrete structures. This report documents improvements made to Grizzly's ability to address both of these structural systems.

For RPVs, the reduced-order models (ROMs) used in fracture mechanics calculations have been expanded to allow their application over a broader range of the parameter space than was permitted by the previous models. The ROMs currently used in Grizzly for the evaluation of flaws that are fully embedded within the RPV (as opposed to surface-breaking flaws) are based on a model that is known to be conservative, indicating higher stress intensity factors than would be obtained from direct simulations. A more accurate model that eliminates these excess conservatisms has been recently included in the American Society of Mechanical Engineers Boiler and Pressure Vessel Code but was not applicable for flaws near the RPV surface, which is where the most critical flaws are usually located. That model has recently been extended for increased applicability in this near-surface region. The ROMs for embedded flaws in the Grizzly code have been expanded to include these recent extensions, which permit their use in a much broader set of cases than previously possible. Direct 3D simulations have been used to check these ROMs and have shown good agreement in most cases, although there are still some cases that need further investigation. There are considerable benefits to using these these more accurate and less conservative ROMs for embedded flaws. On a benchmark probabilistic fracture mechanics problem tested here, the conditional probability of fracture initiation computed for a population of flaws in a single plate in an RPV decreased by over a factor of 3.

To address aging in reinforced concrete structures, a capability to simulate multiple degradation mechanisms, including alkali-silica reaction and radiation-induced volumetric expansion has been developed in Grizzly over the past several years. This had previously been demonstrated on laboratory-scale specimens but not on full-scale nuclear concrete structures with reinforcement. To demonstrate the applicability of Grizzly to the analysis of large-scale structures of interest, a full 3D model of a representative reinforced concrete structure, including a complex arrangement of reinforcing bars, was developed and demonstrated in Grizzly.

# CONTENTS

# FIGURES

# ACRONYMS

| | |
|---|---|
| ASCE | American Society of Civil Engineers |
| ASME | American Society of Mechanical Engineers |
| ASR | alkali-silica reaction |
| ASTM | American Society for Testing and Materials |
| CPI | conditional probability of fracture initiation |
| DOE | Department of Energy |
| EMDA | expanded materials degradation assessment |
| INL | Idaho National Laboratory |
| LWR | light-water reactor |
| LWRS | Light Water Reactor Sustainability |
| MOOSE | Multiphysics Object-Oriented Simulation Environment |
| PFM | probabilistic fracture mechanics |
| PTS | pressurized thermal shock |
| PWR | pressurized-water reactor |
| RIVE | radiation-induced volumetric expansion |
| ROM | reduced-order model |
| RPV | reactor pressure vessel |
| SIF | stress intensity factor |
| SIFIC | stress intensity factor influence coefficient |
| WF | weight function |
| XFEM | extended finite element method |

# 1 Introduction

The materials that make up nuclear power plants are exposed to harsh environmental conditions that can cause accelerated degradation over time. To ensure the continued safe operation of the existing fleet of light-water reactors (LWRs) in the United States, it is important to have tools to predict the progression of aging and assess its effect on the safe operation of those plants. The Grizzly code is being developed for that purpose, with maturing capabilities for assessing the effects of aging on the integrity of reactor pressure vessels (RPVs) and reinforced concrete structures. This report documents work performed to improve and demonstrate the Grizzly code for both of those applications.

## 1.1 Reactor Pressure Vessels

For RPVs, development work focused on development and testing of reduced-order models (ROMs) used in computing fracture mechanics parameters for flaws that are applicable for a broader set of the parameter space than was permitted by the previous models. The probabilistic fracture mechanics (PFM) approach employed by Grizzly uses random sampling to evaluate a large number of potential flaws and determine their likelihood of fracture initiation in aged material under the loading conditions that are expected to occur during a transient event. Three-dimensional (3D) fracture mechanics calculations are very computationally expensive. PFM calculations involve evaluating a large number of potential flaws, and to efficiently perform these calculations, it is essential to use ROMs instead of full 3D fracture mechanics calculations for each flaw.

The ROMs currently used in Grizzly for the evaluation of flaws that are fully embedded within the RPV (as opposed to surface-breaking flaws) are based on a model from an older version of the American Society of Mechanical Engineers (ASME) Boiler and Pressure Vessel Code that is known to be overly conservative. A more accurate model was introduced in the 2015 version of the code, but it only applied to flaws located within the central region of the RPV and is not applicable for flaws near the surface, which are the ones most critical for PFM analyses. Within the last few years, a proposal for an extension of this model to flaws nearer to the surfaces has been published [1], and the recently issued 2021 version of the ASME code incorporates those extensions.

Prior to implementing these models in Grizzly, it is essential to have confidence in their accuracy. A set of direct 3D fracture mechanics calculations has been performed over a subset of the parameter space of these recently proposed ROMs. Grizzly's ROMs have been extended to incorporate the recent proposal for coverage over a broader parameter space, and these ROMs have been tested on a PFM benchmark problem. This effort, which builds confidence both in the ROMs used by Grizzly and in Grizzly's ability to accurately perform direct fracture mechanics calculations, is described in detail in Section 2

## 1.2 Reinforced Concrete Structures

In previous years, a capability to simulate multiple degradation mechanisms, including alkali-silica reaction (ASR) and radiation-induced volumetric expansion (RIVE) was developed in Grizzly, and last year, we demonstrated a set of models for ASR expansion on basic laboratory specimens, including cubes with varying levels of reinforcement and laboratory-scale beams. The intent in development of these capabilities is to apply them for engineering analysis of large-scale nuclear power plant structures. To demonstrate the applicability of Grizzly to such problems, full 3D models have been developed for both an expanded set of laboratory-scale beam specimens and a prototypical nuclear power plant reinforced concrete containment structure. These include complex arrangements of reinforcing bars. These models are described in detail in Section 3.

# 2 Expanded Reduced-Order Models for Reactor Pressure Vessel Fracture Mechanics

The PFM approach employed by Grizzly is detailed in [2] and is based on the algorithms used by the FAVOR code [3]. To evaluate the probability of failure of the RPV under transient conditions, populations of potential flaws are randomly sampled and evaluated. This requires computing the mode-$I$ stress intensity factor ($K_I$) for each flaw during each step of the transient calculation. To directly compute $K_I$ requires evaluating fracture integrals on refined 3D finite element models, which can be very computationally intensive and would not be feasible for the large number of flaws that are evaluated in PFM computations.

The use of ROMs for these fracture calculations is critical for making them computationally feasible. A few key assumptions make it possible to use ROMs for this purpose:

- Linear elastic fracture mechanics is applicable to RPV fracture.
- Flaws can be approximated as having an elliptical or semi-elliptical shape.
- Flaws can be assumed to be aligned with the primary axial or cylindrical coordinates of the RPV.

The ASME Boiler and Pressure Vessel (B&PV) code has long provided methodologies that prescribe ROMs to compute $K_I$ for elliptical (embedded) or semi-elliptical (surface-breaking) flaws. These are provided in Nonmandatory Appendix A, Article A-3000, of Section XI of the code. These ROMs have evolved over the years to include an increasingly complete set of conditions. The current (2021) version of the code [4] provides closed-form equations that cover the full set of cases of interest for surface-breaking flaws. However, the equations for embedded flaws are still under development. Until recently, these did not cover important regions of interest that are critical for PFM calculations and still have some important limitations in their applicability.

The effort documented here tests the ASME code solutions in regions where solutions were recently added. When the present work was initiated, these solutions were not yet incorporated into the code. An independent evaluation of those solutions was necessary before adopting those models. This evaluation serves to verify the accuracy of both Grizzly's ability to directly evaluate these ROMs and the ROMs themselves.

## 2.1 Reduced-Order Model Methodology

The ROM approach for computing fracture parameters in RPV flaws is based on the weight function (WF) approach originally proposed by Buckner [5]. In the general form of this approach, $K_I$ can be expressed as a linear combination of the products of a set of stress coefficients $w_i$ and corresponding stress intensity factor influence coefficients (SIFICs) $K_i$:

$$K_I = \sum_i^n w_i K_i \tag{1}$$

where $w_i$ is a coefficient multiplied by a "load system," or far-field stress state, and $K_i$ is the stress intensity factor (SIF) resulting from the application of load system $i$. The choice of load systems is fairly arbitrary, but in practice, polynomials describing the through-wall variation of the stress as a function of the radial position in the wall are typically used. The form of this expression typically used when polynomials define the load system is:

$$K_I = \sum_i^n C_i K_i \sqrt{\pi a} \tag{2}$$

where $C_i$ are the coefficients of the $i$th term of a polynomial expressing the through-wall variation in the component of the stress perpendicular to an axis-aligned flaw, and $a$ is a dimension of the flaw, as illustrated in Figure 1. This expression is used as the basis of the SIFICs used in the present work.

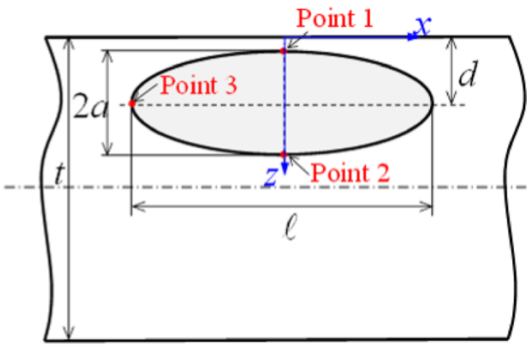


Figure 1. Schematic for embedded elliptical flaw showing parameters used to define the geometry of the flaw. [1]

## 2.2 Summary of Reduced-Order Models for Embedded Flaws

ASME B&PV code has long provided methodologies that prescribe ROMs to compute $K_I$ for elliptical (embedded) or semi-elliptical (surface-breaking) flaws. These are provided in Nonmandatory Appendix A, Article A-3000, of Section XI of the code. These ROMs have evolved over the years to cover an increasingly complete coverage of the full parameter space. The current (2021) version of the code [4] provides closed-form equations that cover the full set of cases of interest for semi-elliptical, axis-aligned, surface-breaking flaws.

The models for flaws that are fully embedded in the wall are still not as complete as those for surface-breaking flaws in the ASME code. In the 2013 and earlier versions of the code, the model for these embedded flaws, referred to as subsurface flaws in the code, was not based on SIFICs and a polynomial expansion of the stress like the surface flaws but was instead based on the stresses perpendicular to the flaw evaluated at Points 1 and 2 in Figure 1. These were used to compute membrane and bending stresses, which were multiplied by factors that were obtained by looking up values from plots. A numerical approach to provide these factors, which facilitates the implementation of this procedure in a computational code, is described in [6].

This approach taken in the code up to 2013 is known to produce overly conservative values for $K_I$. In the 2015 version of the ASME code, this was replaced by a SIFIC-based approach that uses a polynomial expansion of the through-wall stress variation. As indicated in the code, the intent is to eventually provide analytical expressions for the SIFICs, similar to those used for surface-breaking flaws, but currently, a set of lookup tables are used to provide coefficients used in computation of the SIFICs. The parameters used in defining the flaws for these lookup tables are the flaw through-wall radial dimension, $a$, the flaw width, $l$, the depth to the center of the flaw, $d$, and the wall thickness, $t$. The tables provide coefficients in terms of the aspect ratio, $a/l$, the ratio of the depth to thickness, $d/t$, and the ratio of flaw dimension to depth, $a/d$. In the 2015 version of the code, the tables provided values for a limited subset of the parameter space. Values were provided for $a/d$ from 0.0 to 0.8, for $d/t$ from 0.2 to 0.5, and $a/l$ from 0 to 0.5. Interpolation is permitted between the values provided for discrete flaw dimensions provided in those tables.

The coverage provided by these tables in the 2015 code was adequate for the full range of the aspect ratios of interest, ranging from circular to infinite flaws. However, the coverage for $a/d$ and $d/t$ was inadequate for a significant portion of the parameter space of interest for Grizzly PFM calculations. In an RPV, the neutron fluence is highest near the inner surface, so the material in those regions experiences the highest amounts of embrittlement. Additionally, the thermal stresses from cool-down transients are highest in those areas, so the flaws most likely to be locations for fracture initiation tend to be clustered in these areas, as illustrated

in [2]. The lower bound for $d/t$ of 0.2 in the lookup tables meant that flaws on the inner and outer 20% of the RPV were not covered. It should be noted that the upper bound of 0.5 for $d/t$ is not an issue, because for flaws in the outer half of the RPV, the stress coefficients can be re-cast in terms of the distance from the outer surface. In addition to the issues with the range for $d/t$, the upper bound of $a/d$ limits the ability of the model to address flaws whose innermost point is near the RPV surface. Figure 2 illustrates the limited region of applicability of the embedded flaw models in the 2015 ASME code.

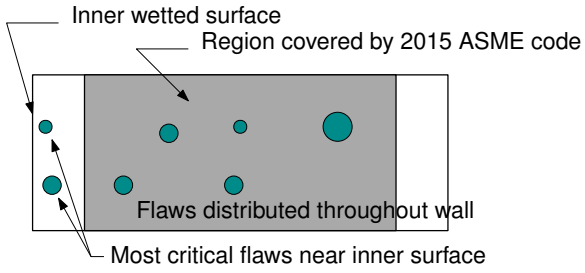


Figure 2. Illustration of the limited region within the RPV wall where embedded flaw models in the 2015 ASME code are applicable.

Despite these limits on the applicable range for this newer approach, there are considerable potential benefits of adopting these models for the regimes for which they are applicable because of the reduced conservatism. Grizzly originally used the pre-2015 procedure for embedded flaws, which is still used as the baseline approach. The 2015 ASME procedure was implemented as an option for cases in its range of applicability in a prior year. In the present year, efforts were focused on expanding the range of applicability of these models in Grizzly.

A recent publication by Lu et al. (2018) [1] proposed an extension of the lookup tables in the ASME code to allow for $d/t$ to range from 0.01 to 0.5. This was accomplished by providing additional sets of values for $d/t = 0.01$ and 0.1, which can be used together with the values that were already provided by the ASME code for $d/t = 0.2$ and greater to interpolate across a much larger region of the parameter space of interest. The proposed values in the tables were based on detailed finite element calculations of flaws with the discrete sets of parameters for the values in the tables.

There are clear benefits to adopting these extensions to the lookup tables for Grizzly because this provide much-improved coverage for flaws located in the critical near-surface regions. However, prior to adopting these models, it is important to develop confidence in these values through independent evaluation. The procedure outlined in Section 2.3 was used to perform independent direct calculations of specific flaw geometries. Section 2.4 presents results from applying that procedure to a subset of the space covered by the combination of the models in [1] and in the 2015 ASME code.

It is important to note that, since the time these independent evaluations were initiated, the 2021 version of the ASME code was released, and this version of the code adopts the expanded models proposed by Lu et al. (2018) without modification. Thus, the combination of the Lu et al. (2018) and 2015 ASME models studied here is identical to the 2021 ASME code.

## 2.3 Direct Simulation Approach for Testing Reduced-Order Models

To compute SIFICs for a given flaw, the geometry requires direct fracture mechanics evaluations of a model that can accurately compute the local stress response in the vicinity of the flaw and perform fracture integrals based on those results. This requires the use of full 3D models for most geometries, although 2D models can be used for flaws with infinite aspect ratios. Finite element models are typically used for this purpose.

The full set of load systems for which SIFICs are desired are applied, and the SIFICs are obtained from the values of $K_I$ under each load system. To perform these analyses, a finite element code must have the ability to apply the appropriate boundary conditions for the load systems, represent the effect of the flaw on the mechanical response, and evaluate the SIFs. Grizzly has this set of capabilities, which were developed as documented in [7] to evaluate both axis-aligned and off-axis flaws.

The current study is limited to axis-aligned flaws, which can be evaluated using a simplification of the same procedure used for off-axis flaws. A brief summary of the aspects of these simulations is provided here. As part of the present work, this approach has been refined as noted to improve the accuracy of the evaluation of the higher order SIFICs. This approach employs a finite element model of a segment of the RPV, such as that shown in Figure 3. Details of this approach are outlined below.

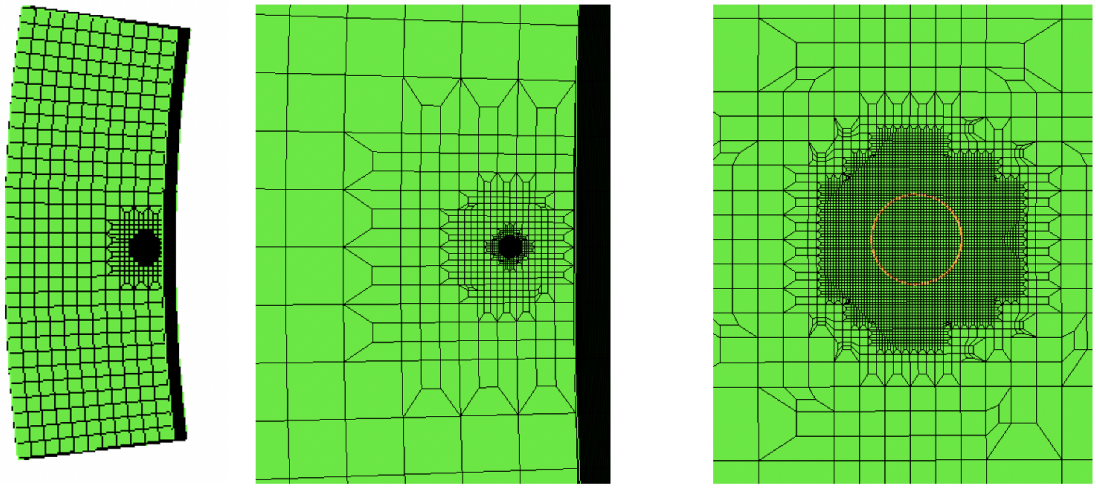

Figure 3. 3D mesh of RPV wall segment for direct evaluation of SIFICs for a specific flaw. The full model is shown (left), as well as zoomed-in views showing local mesh detail (center and right) in the vicinity of the flaw, which is a circumferential flaw in this case.

### 2.3.1 Boundary Conditions

The boundary conditions applied to the model are those that result in the far-field stress away from the crack varying according to the desired term in the polynomial. For a plate geometry, this can be accomplished by either applying the spatially-varying traction at the far boundary of the specimen or by applying the same traction, but in the opposite direction, to the crack face. Traditionally, the traction is applied to the crack face. However, as described in [7], in the code implementation being used, it was more straightforward to apply far-field boundary conditions for general off-axis flaws. For cylindrical geometries, a combination of eigenstrains and body forces are applied to achieve the desired far-field stress conditions. The same approach used previously for off-axis flaws is employed here for axis-aligned flaws, except that only a subset of the loading directions need to be considered for axis-aligned flaws.

### 2.3.2 Representations of Flaws

To avoid the complexities of making a mesh that conforms to the flaw geometry, the extended finite element method (XFEM) [8] is used here to include the discontinuity introduced by the flaw in the displacement field. The XFEM introduces jump discontinuities across elements cut by the plane of the crack, and can also introduce higher order enrichments near the crack tip. As described in [7], Grizzly has the ability to include both types of discontinuities. However, in the present work, near-tip enrichment is not used. Regardless of whether near-tip enrichment is used, some amount of mesh refinement is required in the region of the crack. Near-tip enrichment alleviates that need to some extent. However, there are still some efficiency issues to resolve with that implementation in Grizzly, because the way the code is currently set up, the tip enrichment degrees of freedom exist everywhere in the solution domain, not just near the crack tip. The additional computational expense of using a more refined mesh near the crack tip is somewhat equivalent to the additional expense of using near-tip enrichment.

### 2.3.3 Stress Intensity Factor Evaluation

The interaction integral [9, 10] is used here to compute the mode-$I$ SIFs at points along the crack front. This involves computing an integral of terms involving products of the stress and auxiliary stress, displacement, and strain fields obtained from the solutions for the asymptotic behavior of those fields near the crack tip. These integrals are performed in a post-processing step over a ring-shaped volume around the crack tip. The basic form of the interaction integral $I$ for a point $s$ along the crack front is expressed as [10]:

$$I(s) = \int_V \left[\sigma_{ij} u^{\text{aux}}_{j,1} + \sigma^{\text{aux}}_{ij} u_{j,1} - \sigma_{jk} \epsilon^{\text{aux}}_{jk} \delta_{1i}\right] q_{,i} \, \mathrm{d}V \tag{3}$$

In this equation, $\sigma$ and $u$ are the stress and displacement obtained from the finite element solution, and $q$ is a function that equals 1 inside the inner radius of the integration domain and decreases to 0 at the outside of that ring.

The interaction integral is expressed in terms of the mixed-mode stress intensity factors as:

$$I(s) = \frac{1-\nu^2}{E}\left(2K_I K^{\text{aux}}_I + 2K_{II} K^{\text{aux}}_{II}\right) + \frac{1+\nu}{E}\left(K_{III} K^{\text{aux}}_{III}\right) \tag{4}$$

To obtain individual stress intensity factors, the interaction integral is evaluated with different auxiliary fields. For instance, by choosing $K^{\text{aux}}_I = 1.0$ and $K^{\text{aux}}_{II} = K^{\text{aux}}_{III} = 0$ and computing $I(s)$ in Equation 3, $K_I$ can be solved for in Equation 4.

The expression for the interaction integral in Equation 3 neglects body forces and thermal gradients. The expanded form of this integral, based on [9] includes additional terms for those contributions. These last two terms are included here to account for gradients in the imposed eigenstrain and body forces:

$$\bar{I}(s) = \int_V \left[\sigma_{ij} u^{(aux)}_{j,1} + \sigma^{(aux)}_{ij} u_{j,1} - \sigma_{jk} \epsilon^{(aux)}_{jk} \delta_{1i}\right] q_{,i} \, \mathrm{d}V + \int_V \left[\epsilon^{*}_{ij,1} \sigma^{(aux)}_{ij} - b_i u^{(aux)}_{i,1}\right] q \, \mathrm{d}V \tag{5}$$

where $\epsilon^*$ is the eigenstrain tensor and $b$ is the vector of body forces.

## 2.4 Testing of Reduced-Order Models Using Direct 3D Simulation

The procedure described in the previous section was applied to study a representative subset of the cases provided for flaws near the surface for both the Lu et al. (2018) and 2015 ASME code SIFICs. The representative set of scenarios that were modeled for this study are all circular flaws with an aspect ratio $a/l$ of 0.5. Three relative depths were considered: $d/t = 0.01$, 0.1, and 0.2. The first two are the values of $d/t$ provided

by Lu et al. (2018), while the third is the most shallow relative depth provided by the 2015 ASME code. For each of these depths, the full set of values of the flaw size to depth in the tables were considered: $a/d = 0.1$, 0.2, 0.4, 0.6, and 0.8. Both axial and circumferential orientations were analyzed. The direct fracture model provides solutions for points along the crack front, but the primary point of interest is Point 1 from Figure 1, or the point closest to the inner surface of the RPV. SIFICs values for this point are compared between the published values and those from the present simulations.

Each of the models created for this analysis represents the same solution domain: a 15 degree section of RPV with an inner diameter of 2.1971 m, a thickness of 0.21971 m, and a height of 0.5 m. The axial or circumferential flaw is located in the azimuthal center of this model domain, with varying depth and dimension to cover the set of parameters mentioned previously. The meshes were created using the Cubit meshing software developed at Sandia National Laboratories. The domain is initially meshed using a uniform element size of approximately 0.02 m. The mesh is then refined in the area near the flaw in order to reach a sufficient mesh density for an accurate solution. Because each flaw considered here has different dimensions, a separate mesh is generated for each flaw analysis. The mesh shown in Figure 3 shows the degree of refinement used in the vicinity of the flaw for a representative case. More refined meshes were used for the flaws to ensure an adequately small mesh relative to the size of the flaw. The meshes for the smaller flaws had as many as 2,100,000 elements, while the models with larger flaw sizes had anywhere from 100,000–500,000 elements.

The mesh for each case was developed in a way that ensured that sufficient refinement was provided in the vicinity of the flaw. Figure 4 shows a section view through a typical circumferential flaw and the resulting stress field under uniform axial loading and illustrates the degree of mesh refinement used in the vicinity of the flaw.

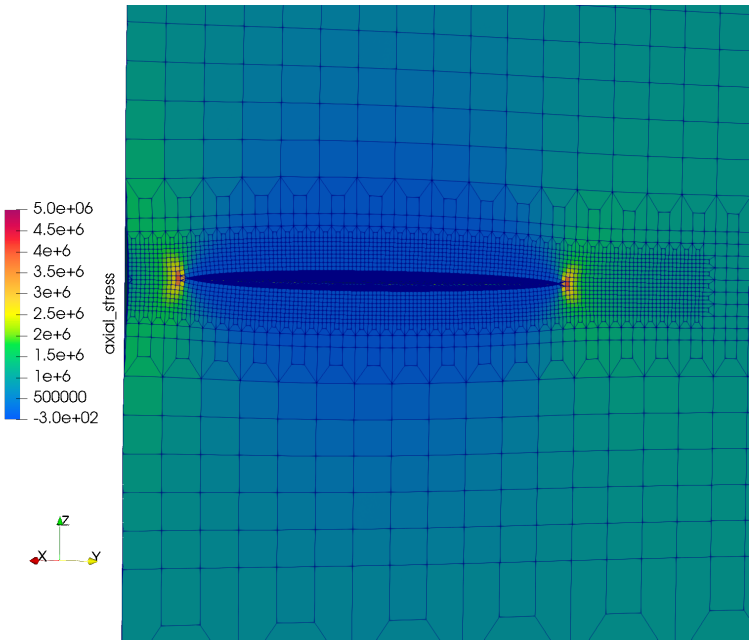


Figure 4. Stress state for a representative circumferential flaw under uniformly applied far-field loading.

The SIF is computed at 80 points around the circumference of the crack front. The number of points is a user-selectable parameter, and a higher number of points better represents the curvature of the crack front. The crack front is represented by a set of line segments for the fracture integral, and the combination of the use of these line segments and the XFEM without near-tip enrichment can result in noisy solutions for the variation of the SIF as a function of position along the crack. The noisiness of these results decreases

with mesh refinement, but using excessively refined meshes would incur high computational expenses for the large number of flaws evaluated here.

A smoothing technique using Gaussian kernels was employed to mitigate this noise in the stresses on these models with moderate levels of mesh refinement. Typically, given $N$ noisy stress outputs, a Gaussian kernel between the current output $Y_0$ and a neighboring output $Y_i$ is defined as [11]:

$$\mathcal{K}(Y_0,\ Y_i) = \exp\left( -\frac{(Y_0 - Y_i)^2}{2\,\sigma^2} \right) \tag{6}$$

where $\sigma$ is the standard deviation of the Gaussian which controls the degree of smoothing. For smoothing the current output $Y_0$, we computed a weighted average across all the outputs using the Nadaraya-Watson estimator [11]. This weighted average for output $Y_0$ or its smoothed value $\hat{Y}_0$ is given by:

$$\hat{Y}_0 = \frac{\sum_{i=1}^{N} \mathcal{K}(Y_0,\ Y_i)\, Y_i}{\sum_{i=1}^{N} \mathcal{K}(Y_0,\ Y_i)} \tag{7}$$

We repeat the process of computing weighted averages using the neighboring points for all the $N$ output values. Also, the larger the $\sigma$ value in Equation (6), the smoother the output would be.

Multiple $\sigma$ values were applied to smooth the computed SIF to understand the effect of that parameter choice. Figure 5 shows the raw values for the SIF as a function of the position on the flaw, as well as the filtered result using $\sigma$ values of 0.5, 1.0, 3.0, and 6.0 for a representative flaw under the five loading conditions corresponding with the five coefficients in the polynomial for the through-wall stress variation. For each of these cases, the loading conditions result in a maximum far-field stress of 1 MPa, but the through-wall stress field varies according to a different term in the polynomial. It is evident that smoothing significantly reduces the noise, and gives improved results for the point on the flaw nearest to the inner surface, which is the point in the center (with a position index equal to 41) in each case. From these results, $\sigma = 3.0$ gives an optimal smoothing, and that value is used in all cases. The values of the SIF at that position are used to compute the SIFICs, which are shown in Table 1 with and without smoothing for this case. Results are compared with the solutions from Lu et al. (2018), and it is evident that the smoothing significantly reduces the error.

Table 1. SIFICs from a representative case (d/t = 0.1, a/d = 0.2) with and without the Gaussian smoothing applied to the results.

| Coefficient | Raw | Lu | Error % | Smoothed | Lu | Error % |
|---|---|---|---|---|---|---|
| G0 | 0.9342 | 0.9813 | 5.04 | 0.9931 | 0.9813 | 1.19 |
| G1 | 7.9983E-02 | 8.5040E-02 | 6.32 | 8.5381E-02 | 8.5040E-02 | 0.40 |
| G2 | 6.9100E-03 | 7.4300E-03 | 7.53 | 7.4051E-03 | 7.4300E-03 | 0.34 |
| G3 | 6.0380E-04 | 6.5510E-04 | 8.50 | 6.4933E-04 | 6.5510E-04 | 0.89 |
| G4 | 5.3659E-05 | 5.8350E-05 | 8.74 | 5.7878E-05 | 5.8350E-05 | 0.82 |

This smoothing procedure is applied to all results presented hereafter. As mentioned previously, it would be preferable to use either a more refined mesh or near-tip enrichment to minimize the noise and the need for smoothing, but the smoothing process would still likely improve the results even if that were done.

The $K_I$ solution computed by Grizzly for the point nearest to the inner surface, after applying smoothing, is scaled by the flaw shape parameter as shown below to obtain the SIFIC for a given polynomial term:

$$Q = 1.0 + 4.593(a/l)^{1.65} \tag{8}$$

This operation converts $K_I$ to an SIFIC, which allows a direct comparison with the tabulated values.

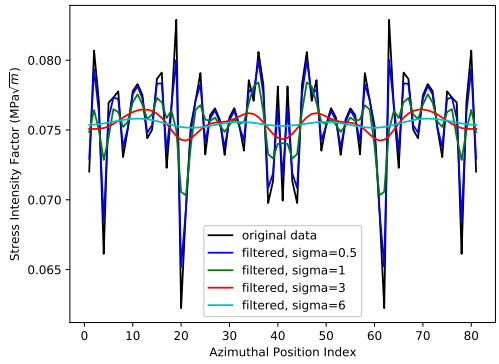


(a) Constant loading (0th order term)

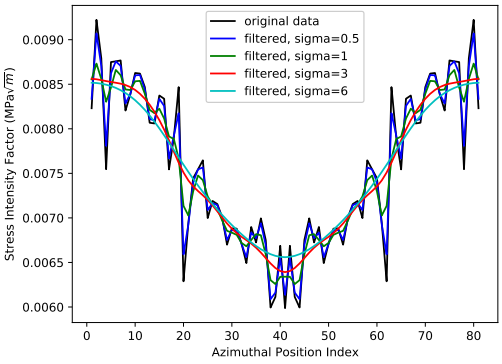


(b) Linear loading (1st order term)

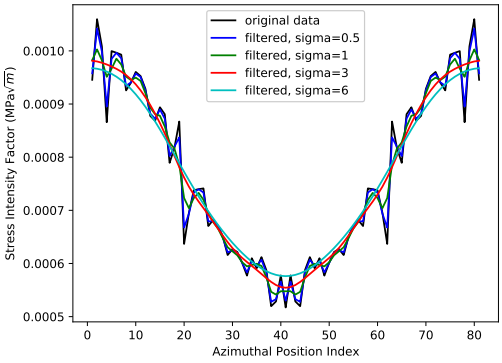


(c) Quadratic loading (2st order term)

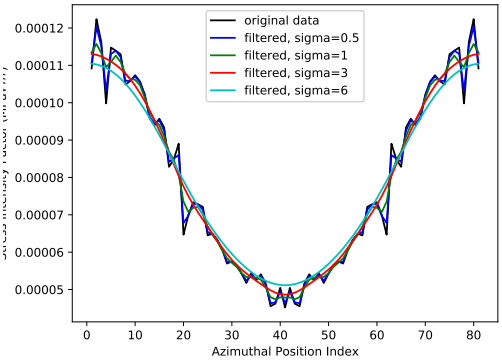


(d) Cubic loading (3rd order term)

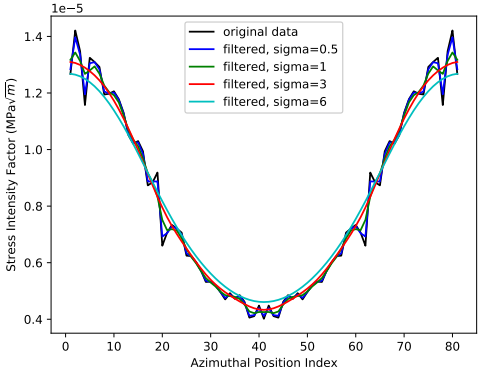


(e) Quartic loading (4rd order term)

Figure 5. SIF vs. azimuthal position for a representative flaw under radially varying far-field stress corresponding to the five terms in the polynomial, illustrating the effects of smoothing with varying values of smoothing parameter $\sigma$. Azimuthal position is shown in terms of the index of the point around the crack front.

The SIFICs computed using direct Grizzly simulations with smoothing, compared to either the Lu et al. (2018) or 2015 ASME solutions, for the full set of cases considered are shown in Tables 2, 3, 4, 5, and 6 for the 0th, 1st, 2nd, 3rd, and 4th order cases, respectively. The columns denoted as "Lu" are those flaws that

fall within the expanded depth region of the RPV wall provided by Lu et al. (2018). The columns denoted as "A3000" are flaws whose $a/d$ dimension is at the lower bound of the 2015 ASME tabulated SIFICs for embedded flaws.

Table 2. SIFICs from uniform loading for both circumferential and axial embedded flaws.

| G1 Point #1 (shallow point) Circumferential Flaw | | | | | | | | | |
|---|---|---|---|---|---|---|---|---|---|
| | d/t = 0.01 | | | d/t = 0.1 | | | d/t = 0.2 | | |
| a/d | Grizzly | Lu | Error % | Grizzly | Lu | Error % | Grizzly | A3000 | Error % |
| 0.1 | 8.2508E-03 | 9.0510E-03 | 8.84 | 9.3728E-02 | 9.1130E-02 | 2.85 | 1.8540E-01 | 1.8640E-01 | 0.54 |
| 0.2 | 8.5980E-03 | 8.4660E-03 | 1.56 | 8.5381E-02 | 8.5040E-02 | 0.40 | 1.7216E-01 | 1.7290E-01 | 0.43 |
| 0.4 | 6.8373E-03 | 7.2320E-03 | 5.46 | 7.2697E-02 | 7.2420E-02 | 0.38 | 1.4539E-01 | 1.4710E-01 | 1.16 |
| 0.6 | 5.9524E-03 | 6.1180E-03 | 2.71 | 6.1154E-02 | 6.1570E-02 | 0.68 | 1.2255E-01 | 1.2560E-01 | 2.43 |
| 0.8 | 5.1284E-03 | 5.4020E-03 | 5.06 | 5.2390E-02 | 5.4550E-02 | 3.96 | 1.0554E-01 | 1.1170E-01 | 5.51 |
| G0 Point #1 (shallow point) Axial Flaw | | | | | | | | | |
| a/d | Grizzly | Lu | Error % | Grizzly | Lu | Error % | Grizzly | A3000 | Error % |
| 0.1 | 8.3274E-03 | 9.0510E-03 | 7.99 | 9.3424E-02 | 9.1130E-02 | 2.52 | 1.8523E-01 | 1.8640E-01 | 0.63 |
| 0.2 | 8.5857E-03 | 8.4660E-03 | 1.41 | 8.5412E-02 | 8.5040E-02 | 0.44 | 1.7229E-01 | 1.7290E-01 | 0.35 |
| 0.4 | 6.8699E-03 | 7.2320E-03 | 5.01 | 7.2764E-02 | 7.2420E-02 | 0.48 | 1.4541E-01 | 1.4710E-01 | 1.15 |
| 0.6 | 5.9623E-03 | 6.1180E-03 | 2.55 | 6.1215E-02 | 6.1570E-02 | 0.58 | 1.2294E-01 | 1.2560E-01 | 2.12 |
| 0.8 | 5.1151E-03 | 5.4020E-03 | 5.31 | 5.2416E-02 | 5.4550E-02 | 3.91 | 1.0611E-01 | 1.1170E-01 | 5.01 |

Table 3. SIFICs from linear loading for both circumferential and axial embedded flaws.

| G2 Point #1 (shallow point) Circumferential Flaw | | | | | | | | | |
|---|---|---|---|---|---|---|---|---|---|
| | d/t = 0.01 | | | d/t = 0.1 | | | d/t = 0.2 | | |
| a/d | Grizzly | Lu | Error % | Grizzly | Lu | Error % | Grizzly | A3000 | Error % |
| 0.1 | 7.6692E-05 | 8.4580E-05 | 9.33 | 8.7408E-03 | 8.5200E-03 | 2.59 | 3.4546E-02 | 3.4800E-02 | 0.73 |
| 0.2 | 7.4634E-05 | 7.3940E-05 | 0.94 | 7.4051E-03 | 7.4300E-03 | 0.34 | 2.9954E-02 | 3.0200E-02 | 0.82 |
| 0.4 | 5.0964E-05 | 5.5570E-05 | 8.29 | 5.5435E-03 | 5.5650E-03 | 0.39 | 2.2117E-02 | 2.2600E-02 | 2.14 |
| 0.6 | 4.0916E-05 | 4.3050E-05 | 4.96 | 4.3007E-03 | 4.3400E-03 | 0.91 | 1.7168E-02 | 1.7800E-02 | 3.55 |
| 0.8 | 3.6315E-05 | 3.8510E-05 | 5.70 | 3.7204E-03 | 3.8970E-03 | 4.53 | 1.5205E-02 | 1.6300E-02 | 6.72 |
| G0 Point #1 (shallow point) Axial Flaw | | | | | | | | | |
| a/d | Grizzly | Lu | Error % | Grizzly | Lu | Error % | Grizzly | A3000 | Error % |
| 0.1 | 7.7399E-05 | 8.4580E-05 | 8.49 | 8.6956E-03 | 8.5200E-03 | 2.06 | 3.4516E-02 | 3.4800E-02 | 0.82 |
| 0.2 | 7.4671E-05 | 7.3940E-05 | 0.99 | 7.4083E-03 | 7.4300E-03 | 0.29 | 2.9979E-02 | 2.8630E-02 | 4.71 |
| 0.4 | 5.1443E-05 | 5.5570E-05 | 7.43 | 5.5509E-03 | 5.5650E-03 | 0.25 | 2.2124E-02 | 2.2600E-02 | 2.11 |
| 0.6 | 4.1138E-05 | 4.3050E-05 | 4.44 | 4.3070E-03 | 4.3400E-03 | 0.76 | 1.7246E-02 | 1.7800E-02 | 3.11 |
| 0.8 | 3.6450E-05 | 3.8510E-05 | 5.35 | 3.7235E-03 | 3.8970E-03 | 4.45 | 1.5329E-02 | 1.6300E-02 | 5.96 |

There is generally good agreement between the Grizzly results obtained through direct 3D simulation and the Lu et al. (2018) and ASME 2015 solutions. In most cases, the relative errors between the solutions are less than around 5%. This is an important confirmation both of Grizzly's ability to directly compute fracture parameters for arbitrary flaw geometries and of the accuracy of the tabulated SIFICs. However, there are a few cases with larger discrepancies. The case with $a/d = 0.1$ and $d/t = 0.01$ shows a relative error of about 10% for all terms in the polynomial. Also, for all of the Lu et al. (2018) solutions with $d/t = 0.01$, the errors are significant for the 3rd and 4th order SIFICs. Interestingly, the errors for those cases for the lower order terms are minimal and in line with the errors for the deeper flaw cases.

The tabulated solutions of Lu et al. (2018) and the 2015 ASME code do not differentiate between axial and circumferential flaws, and there is little difference between the Grizzly solutions for these two cases, which confirms that there is no need for separate solutions. The circumferential flaws account for the effect of the curvature of the RPV wall, which is shown here to have a minimal effect for embedded flaws. The Grizzly solutions for the axial flaws are generally slightly closer to the tabulated solutions, which is intuitive

Table 4. SIFICs from quadratic loading for both circumferential and axial embedded flaws.

| G3 Point #1 (shallow point) Circumferential Flaw | | | | | | | | | |
|---|---|---|---|---|---|---|---|---|---|
| | d/t = 0.01 | | | d/t = 0.1 | | | d/t = 0.2 | | |
| a/d | Grizzly | Lu | Error % | Grizzly | Lu | Error % | Grizzly | A3000 | Error % |
| 0.1 | 1.7042E-06 | 7.9180E-07 | 115.23 | 8.1763E-04 | 7.9780E-04 | 2.49 | 6.4501E-03 | 6.5000E-03 | 0.77 |
| 0.2 | 1.3501E-06 | 6.5170E-07 | 107.16 | 6.4933E-04 | 6.5510E-04 | 0.88 | 5.2630E-03 | 5.4000E-03 | 2.54 |
| 0.4 | 1.1243E-06 | 4.5030E-07 | 149.67 | 4.4823E-04 | 4.5100E-04 | 0.61 | 3.5561E-03 | 3.7000E-03 | 3.89 |
| 0.6 | 1.4272E-06 | 3.5370E-07 | 303.49 | 3.5599E-04 | 3.5720E-04 | 0.34 | 2.8172E-03 | 3.0000E-03 | 6.09 |
| 0.8 | 1.7555E-06 | 3.5960E-07 | 388.19 | 3.4418E-04 | 3.6450E-04 | 5.57 | 2.8341E-03 | 3.1000E-03 | 8.58 |
| G0 Point #1 (shallow point) Axial Flaw | | | | | | | | | |
| a/d | Grizzly | Lu | Error % | Grizzly | Lu | Error % | Grizzly | A3000 | Error % |
| 0.1 | 1.9496E-06 | 7.9180E-07 | 146.22 | 8.1217E-04 | 7.9780E-04 | 1.80 | 6.4447E-03 | 6.5000E-03 | 0.85 |
| 0.2 | 1.5752E-06 | 6.5170E-07 | 141.71 | 6.4994E-04 | 6.5510E-04 | 0.79 | 5.2683E-03 | 5.4000E-03 | 2.44 |
| 0.4 | 1.4745E-06 | 4.5030E-07 | 227.45 | 4.4930E-04 | 4.5100E-04 | 0.38 | 3.5579E-03 | 3.7000E-03 | 3.84 |
| 0.6 | 1.7694E-06 | 3.5370E-07 | 400.26 | 3.5699E-04 | 3.5720E-04 | 0.06 | 2.8348E-03 | 3.0000E-03 | 5.51 |
| 0.8 | 2.1647E-06 | 3.5960E-07 | 501.98 | 3.4488E-04 | 3.6450E-04 | 5.38 | 2.8642E-03 | 3.1000E-03 | 7.61 |

Table 5. SIFICs from cubic loading for both circumferential and axial embedded flaws.

| G4 Point #1 (shallow point) Circumferential Flaw | | | | | | | | | |
|---|---|---|---|---|---|---|---|---|---|
| | d/t = 0.01 | | | d/t = 0.1 | | | d/t = 0.2 | | |
| a/d | Grizzly | Lu | Error % | Grizzly | Lu | Error % | Grizzly | A3000 | Error % |
| 0.1 | 3.7673E-07 | 7.4270E-09 | 4972.44 | 7.6909E-05 | 7.4850E-05 | 2.75 | 1.2071E-03 | 1.2000E-03 | 0.59 |
| 0.2 | 1.8526E-07 | 5.8020E-09 | 3093.03 | 5.7878E-05 | 5.8350E-05 | 0.81 | 9.3502E-04 | 1.0000E-03 | 6.50 |
| 0.4 | 2.4203E-07 | 3.8660E-09 | 6160.60 | 3.8973E-05 | 3.8720E-05 | 0.65 | 6.0663E-04 | 6.0000E-04 | 1.10 |
| 0.6 | 3.8366E-07 | 3.3330E-09 | 11410.86 | 3.4264E-05 | 3.3710E-05 | 1.64 | 5.2866E-04 | 6.0000E-04 | 11.89 |
| 0.8 | 6.1144E-07 | 3.9560E-09 | 15356.08 | 3.7905E-05 | 4.0150E-05 | 5.59 | 6.1780E-04 | 7.0000E-04 | 11.74 |
| G0 Point #1 (shallow point) Axial Flaw | | | | | | | | | |
| a/d | Grizzly | Lu | Error % | Grizzly | Lu | Error % | Grizzly | A3000 | Error % |
| 0.1 | 5.6794E-07 | 7.4270E-09 | 7546.93 | 7.6415E-05 | 7.4850E-05 | 2.09 | 1.2062E-03 | 1.2000E-03 | 0.52 |
| 0.2 | 4.4240E-07 | 5.8020E-09 | 7525.01 | 5.8173E-05 | 5.8350E-05 | 0.30 | 9.3621E-04 | 1.0000E-03 | 6.38 |
| 0.4 | 5.0820E-07 | 3.8660E-09 | 13045.46 | 3.9292E-05 | 3.8720E-05 | 1.48 | 6.0711E-04 | 6.0000E-04 | 1.19 |
| 0.6 | 6.5028E-07 | 3.3330E-09 | 19410.43 | 3.4591E-05 | 3.3710E-05 | 2.61 | 5.3297E-04 | 6.0000E-04 | 11.17 |
| 0.8 | 9.1974E-07 | 3.9560E-09 | 23149.23 | 3.8221E-05 | 4.0150E-05 | 4.80 | 6.2564E-04 | 7.0000E-04 | 10.62 |

because those solutions were likely based on axial flaws.

Most of the differences between the Grizzly solutions and the tabulated SIFICs are generally not concerning. Where there are discrepancies, the Grizzly solutions are lower in almost all cases, and it is likely that with increased mesh refinement, the solutions would be closer. However, the discrepancies in the 3rd and 4th order terms for $d/t = 0.01$ are concerning because the tabulated solutions are orders of magnitude lower than the Grizzly solutions. Because the contributions of these higher order terms are generally minor, this would have a minimal effect on the solutions in many cases, but this should be further investigated. Additional evaluations of flaws in the regimes between $d/t = 0.1$ and 0.01 would be helpful for understanding this behavior.

## 2.5 Incorporation of Expanded Reduced-Order Models in Grizzly

Prior to the present effort, Grizzly had a capability to use both the methods in the 2013 and earlier ASME code and the 2015 ASME code for embedded flaw calculations. However, because the range of applicability of the 2015 code was quite limited, the 2013 and earlier version has been used for essentially all PFM calculations with Grizzly. In the present effort, the SIFIC tables have been extended to incorporate the Lu et al. (2018) solutions for a much more complete coverage of the parameter space.

Table 6. SIFICs from quartic loading for both circumferential and axial embedded flaws.

| G0 Point #1 (shallow point) Circumferential Flaw | | | | | | | | | |
|---|---|---|---|---|---|---|---|---|---|
| | d/t = 0.01 | | | d/t = 0.1 | | | d/t = 0.2 | | |
| a/d | Grizzly | Lu | Error % | Grizzly | Lu | Error % | Grizzly | A3000 | Error % |
| 0.1 | 0.8905 | 0.9706 | 8.25 | 1.0071 | 0.9768 | 3.10 | 0.9969 | 1.0005 | 0.36 |
| 0.2 | 1.0003 | 0.9768 | 2.41 | 0.9931 | 0.9813 | 1.20 | 0.9985 | 1.0012 | 0.27 |
| 0.4 | 0.9571 | 0.9848 | 2.81 | 1.0022 | 0.9866 | 1.58 | 1.0040 | 1.0095 | 0.55 |
| 0.6 | 1.0144 | 1.0070 | 0.74 | 1.0241 | 1.0120 | 1.20 | 1.0288 | 1.0435 | 1.41 |
| 0.8 | 1.0917 | 1.0930 | 0.12 | 1.1080 | 1.1010 | 0.63 | 1.1009 | 1.1389 | 3.34 |
| G0 Point #1 (shallow point) Axial Flaw | | | | | | | | | |
| a/d | Grizzly | Lu | Error % | Grizzly | Lu | Error % | Grizzly | A3000 | Error % |
| 0.1 | 0.8986 | 0.9706 | 7.42 | 1.0060 | 0.9768 | 2.99 | 0.9960 | 1.0005 | 0.45 |
| 0.2 | 0.9987 | 0.9768 | 2.24 | 0.9934 | 0.9813 | 1.24 | 0.9992 | 1.0012 | 0.20 |
| 0.4 | 0.9614 | 0.9848 | 2.38 | 1.0028 | 0.9866 | 1.65 | 1.0041 | 1.0095 | 0.54 |
| 0.6 | 1.0162 | 1.0070 | 0.91 | 1.0249 | 1.0120 | 1.28 | 1.0310 | 1.0435 | 1.19 |
| 0.8 | 1.0892 | 1.0930 | 0.35 | 1.1083 | 1.1010 | 0.66 | 1.1041 | 1.1389 | 3.06 |

### 2.5.1 Code Implementation and Options

In Grizzly PFM calculations, a modular set of code objects is used in the various aspects of the calculation, as described in [2]. This allows for the user to easily select between multiple methods for use in parts of that calculation.

An important component of this fracture calculation is the object that computes $K_I$, which is `KIAxisAlignedROM` for axis-aligned flaws. This object provides options to specify the option used to compute $K_I$ for embedded flaws with the `embedded_sific_method` parameter. The following options are available for this parameter:

- `FAVOR16`: The method used by Version 16.1 of the FAVOR code, which uses the 2013 and earlier versions of the ASME code for embedded flaws.
- `A3000_2015`: The method provided in the 2015 ASME code. If dimensions are outside the provided tables, the code exits with an error.
- `LU_2018`: The combination of the Lu et al. (2018) solutions and the 2015 ASME code (identical to the solutions in the 2021 ASME code). If dimensions are outside the provided tables, the code exits with an error.
- `HYBRID_A3000_2015_FAVOR16`: Identical to the `A3000_2015` option, except that, if a flaw falls outside the interpolation tables, the 2013 and earlier ASME code solutions are used.
- `HYBRID_LU_2018_FAVOR16`: Identical to the `LU_2018` option, except that, if a flaw falls outside the interpolation tables, the 2013 and earlier ASME code solutions are used.

Because in a PFM calculation, some of the randomly-generated flaws always fall outside the bounds of the `A3000_2015` or `LU_2018` models, it is essential in practice to use the hybrid options of those models.

### 2.5.2 Testing

While it is generally desirable for a model to provide conservative results, for probabilistic calculations, such as those performed using these models, it is desirable for all aspects of the model to produce results that are as accurate as possible, with minimal excess conservatism. Thus, adopting the newer models over as large of a range of the parameter space as possible is desirable for Grizzly PFM calculations.

To demonstrate the effects of the updated ROMs on PFM results, a basic benchmark case on a single panel in an RPV subjected to a pressurized thermal shock transient was analyzed. This was done two ways: with the 2013 and earlier ASME model, and with the hybrid model that uses the 2021 ASME model whenever possible and falls back on the 2013 model for cases that are outside the parameter space of the newer model. This problem is based on the single-panel model that was initially developed in [12] and further refined in [13].

In the PFM calculation of that panel, 1,000,000 random realizations of flaw populations were evaluated, which provided adequate convergence of the Monte Carlo solution. In the baseline case with the 2013 ASME model, the computed value of the conditional probability of fracture initiation (CPI) was $9.24 \times 10^{-7}$, while in the case using the hybrid approach with the 2021 ASME model, the CPI was $2.67 \times 10^{-7}$, which indicates that using the more accurate and less conservative models has a significant effect on the results. There is clear motivation to use these updated models and to further extend these models to cover the full parameter space. Within the full set of Monte Carlo samples, around 0.4% of the flaws fell within the regime not covered by the 2021 ASME model. These flaws, which are near the surface of the RPV, are the ones that are most likely to result in fracture initiation, so further extending these models is expected to result in further notable decreases in the computed CPI. This case investigates only a small subset of an RPV and has a relatively low CPI to start with. Further investigation of full RPV models would be necessary to fully understand the impact of using these models.

# 3 Validation and Demonstration of Concrete Degradation Model

To address aging in reinforced concrete (RC) structures, Grizzly has capabilities to model the response of coupled physical phenomena leading to degradation, as well as the progression of degradation mechanisms and their effect on the mechanical response. Incremental improvements to these capabilities have been made over the last several years, and they have reached the point where they are sufficiently complete to model realistic reinforced concrete studies. An initial set of validation cases on simple laboratory specimens has been shown in [12], and the present effort is focused on extending these cases to more complex laboratory specimens and demonstrating an application to simulate ASR in a 3D nuclear containment structure.

## 3.1 Modeling Approach

Modeling the evolution of ASR in a reinforced concrete structure in Grizzly accounts for the temperature, moisture, and state of stress at local material points. In Grizzly, the model of Saouma and Perotti [14] for ASR-induced volumetric strain is used. The model estimates the ASR extent using characteristic time, latency time, compressive strength of concrete, and state of stresses in the domain. The ASR extent is used to obtain the ASR volumetric strain in concrete, which is dependent on the tensile strength of the concrete, maximum principal stress in tension, hydrostatic stress, moisture, and maximum volumetric expansion in laboratory conditions. The model also accounts for the damage in the elastic modulus of concrete by estimating a scalar damage variable, which is dependent on the ASR extent in concrete.

As mentioned earlier, ASR in concrete depends on the temperature and moisture in the concrete domain; therefore, existing models for thermal and moisture transport are implemented and validated using existing experimental studies. The thermal transport model considers the convective heat transport due to fluid flow, the heat of adsorption of free water molecules in pores onto the walls, and volumetric heating. Multiple thermal transport models (Kodur [15], ASCE [16], and Eurocode [17] are included in Grizzly to account for type of aggregates, temperature range, and compressive strength of the concrete. Kodur's and ASCE models account for siliceous and carbonate aggregates. Kodur's model is applicable for high-strength concrete while the ASCE model is applicable for normal strength concrete. The Eurocode model is applicable for both high and normal strength concrete but does not account for the type of aggregate in the concrete mix. All three models are applicable for a wide range of temperatures. Similarly, multiple moisture transport models are included in Grizzly to account for the concrete mix proportion (such as water-cement ratio, aggregate volume fraction, cement type, aggregate type, and aggregate pore type) and the curing and exposure conditions (such as temperature and humidity).These models include Bazant's model [18], Xi's model [19], and Mensi's model [20]. Bazant's model applies to the high-temperature range, Xi's model is applicable for a high water-cement ratio (>0.5), and Mensi's model accounts only for the initial water content in the concrete.

Since the state of stresses affects the ASR-induced volumetric strain, the steel reinforcement arrangement in the reinforced concrete structure needs to be modeled. Steel reinforcement is modeled as trusses. These truss elements are embedded in concrete, which is modeled using 2D or 3D continuum finite elements, using constraints that enforce equivalence in the displacement field between the truss nodes and the points where they are located in the continuum elements. The use of these constraints allows the rebars and concrete to be meshed independently, so they do not need to share nodes.

## 3.2 Modeling of Reinforced Concrete Beam Members

The first part of the present effort consisted of developing additional validation cases of laboratory-tested concrete beams. Three reinforced concrete beam members [21] are considered for this purpose and model ASR-induced expansion, as shown in Figure 6. Beam 4 in Figure 6 was subjected to the laboratory environment, while Beam 5 and Beam 6 were subjected to the ambient environment in Los Angeles, CA. Beam 4

and Beam 5 were constructed using the same batch of concrete with no alkali content in them, while Beam 6 had an alkaline solution, which is 1.25% by weight of cement. Relevant experimental information are presented in Table 7 and other experimental details can be found in the already published report [21]. The beams are designed to have two shear spans to perform two mechanical testings. From the ASR perspective, the beams can be divided into two zones based on the confinement: heavy confinement (middle span) and light confinement (left and right shear span).

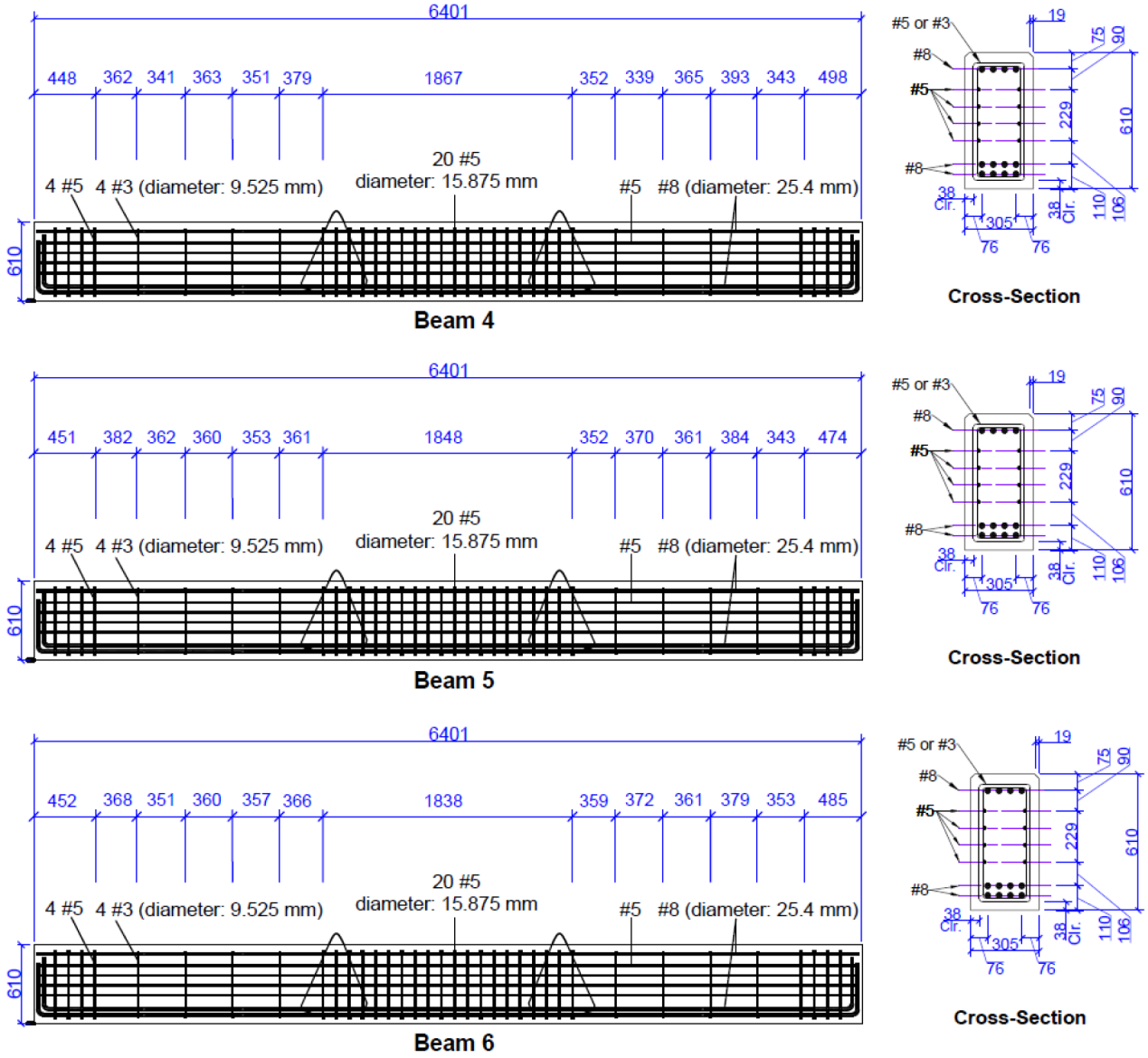


Figure 6. Reinforced concrete beams used for ASR study.

The Grizzly finite element model of this beam is shown in Figure 7. The beam model is divided into three blocks corresponding to the shear span in the left and right part of the beam and the heavy confinement region in the middle part of the beam. The modeling parameters for the beam are indicated in Table 9. All blocks are subjected to the same temperature and relative humidity boundary conditions as observed during

Table 7. Mix proportion of concrete and properties of RC beam.

| **Material/Parameter** | **Properties/Quantity** |
|---|---|
| Cement | Type II/IV low alkali Portland cement (alkali content $< 0.6\%$) |
| Coarse Aggregate | 3/4" and 3/8" aggregate (crushed rock) |
| Fine Aggregate | Reactive from El Paso (mortar bar test shows 0.6% and 0.8% ASR expansion at 16 days and 25 days, respectively) |
| $f_c^{'}$ at 28 Days | 38 MPa, 37 MPa, and 34 MPa for concrete batches corresponding to Beam 4, Beam 5, and Beam 6, respectively. |

the exposure period in the experiment. The temperature and relative humidity in the beam are monitored throughout the experimental period. The location of temperature and relative humidity sensors are shown in Figure 8. Experimentally observed temperature and relative humidity are compared to those values obtained from the simulation in Figure 9 and Figure 10, respectively. The temperature profile in Beam 4 is accurately predicted from the simulation whereas those in Beam 5 and Beam 6 differ significantly. Similar results are obtained for the relative humidity.

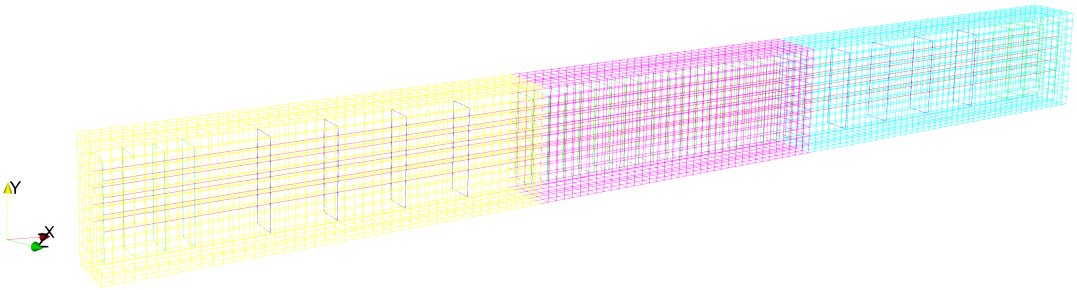


Figure 7. Reinforced concrete beams model used in Grizzly.

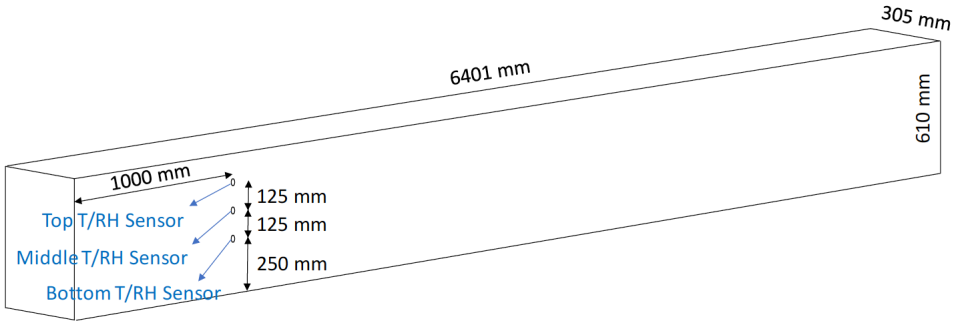


Figure 8. Locations of temperature and relative humidity sensors in reinforced concrete beams.

ASR expansion from the simulation of Beams 4, 5, and 6 are compared with that from the experimental results from [21] in Figure 11. Experimental results in Figure 11 are plotted with mean and single standard

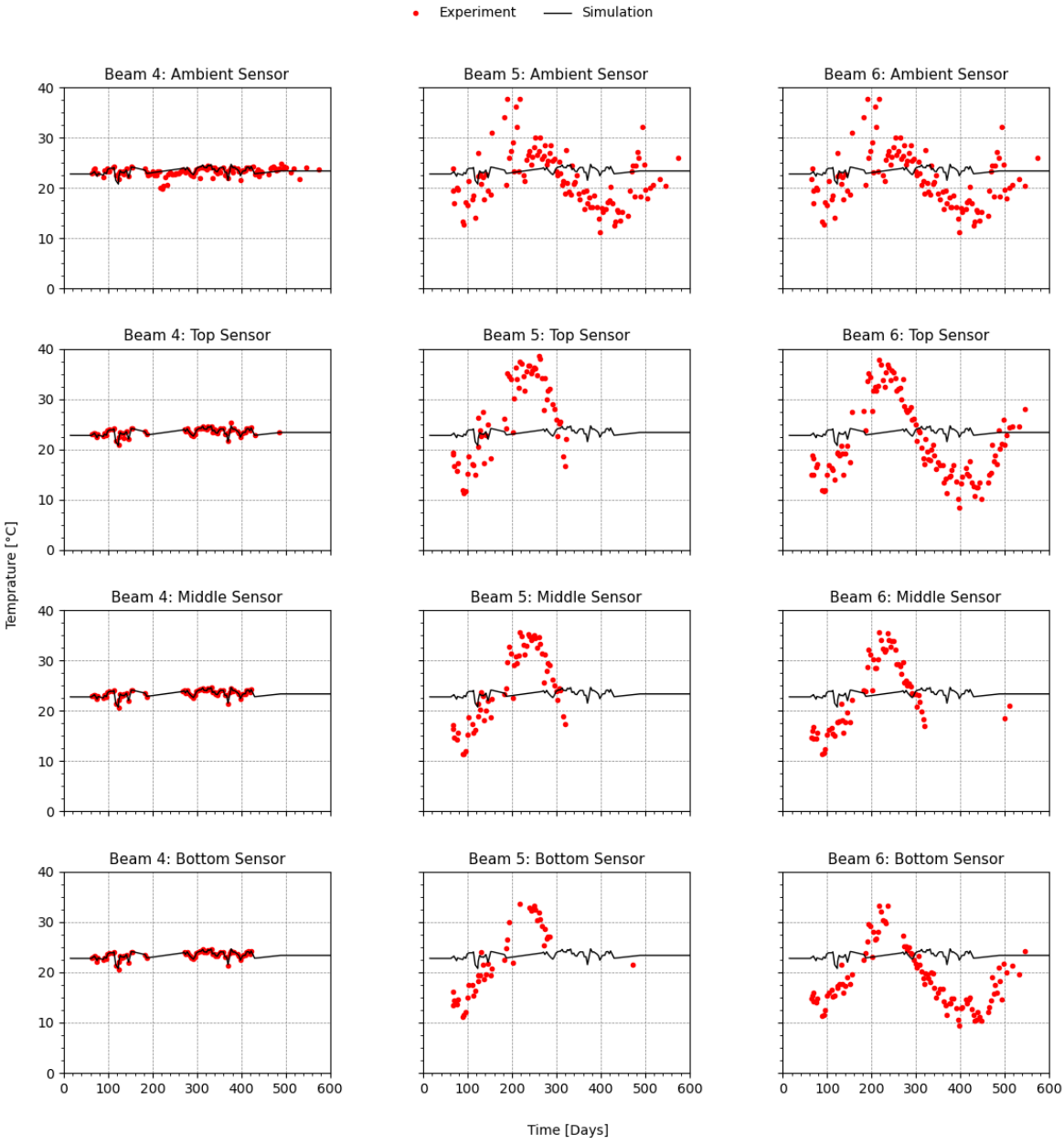


Figure 9. Comparison of experimentally-observed and simulation-obtained temperature in the beams.

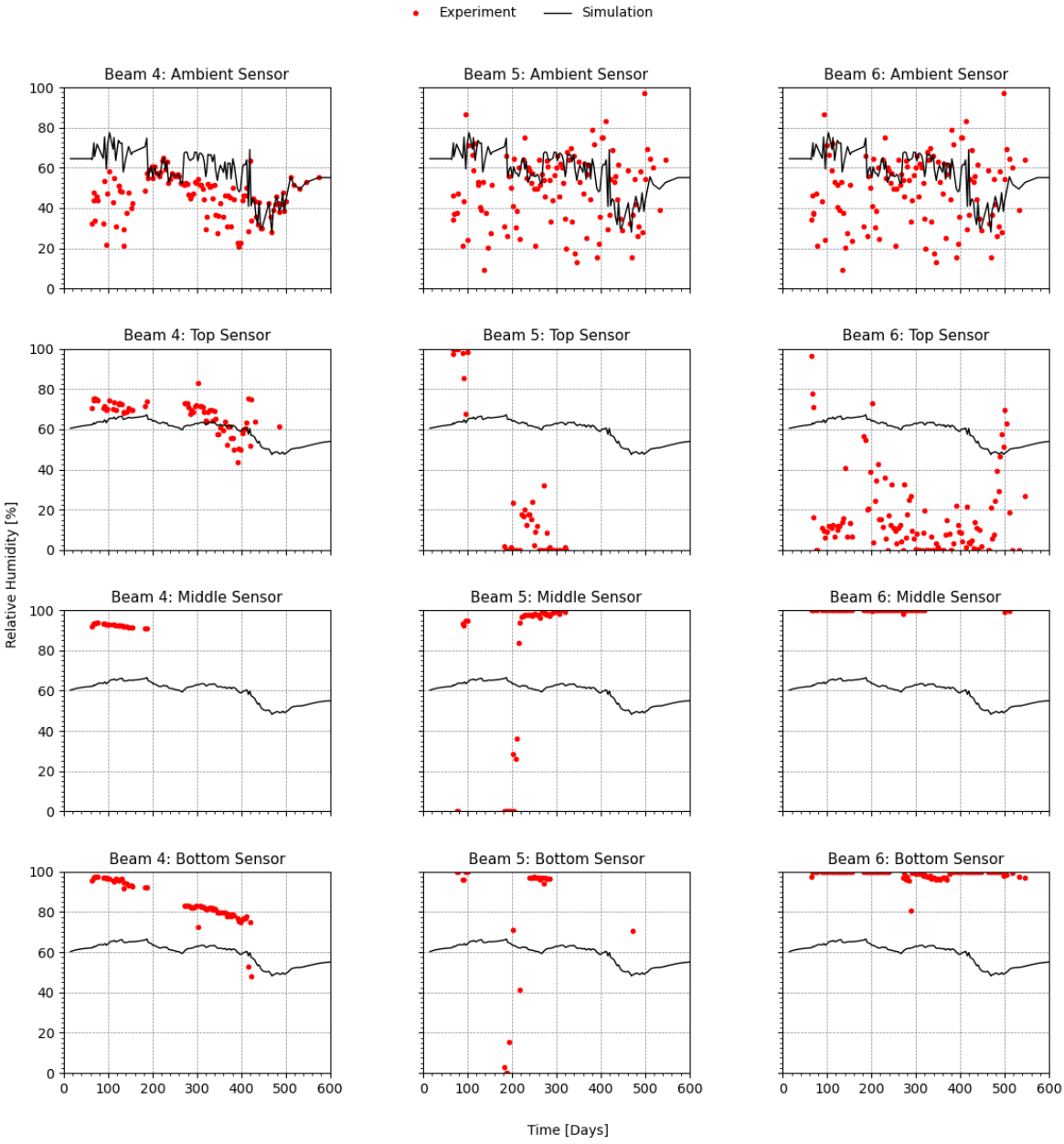


Figure 10. Comparison of experimentally-observed and simulation-obtained relative humidity in the beams.

deviation. The simulations predict the ASR expansion along each direction reasonably well for the entire duration of the experiment. The volumetric ASR expansion is compared in Figure 12 for the aforementioned two regions in the beams. The volumetric expansion is observed more in the shear span due to lower confinement as compared to the middle span.

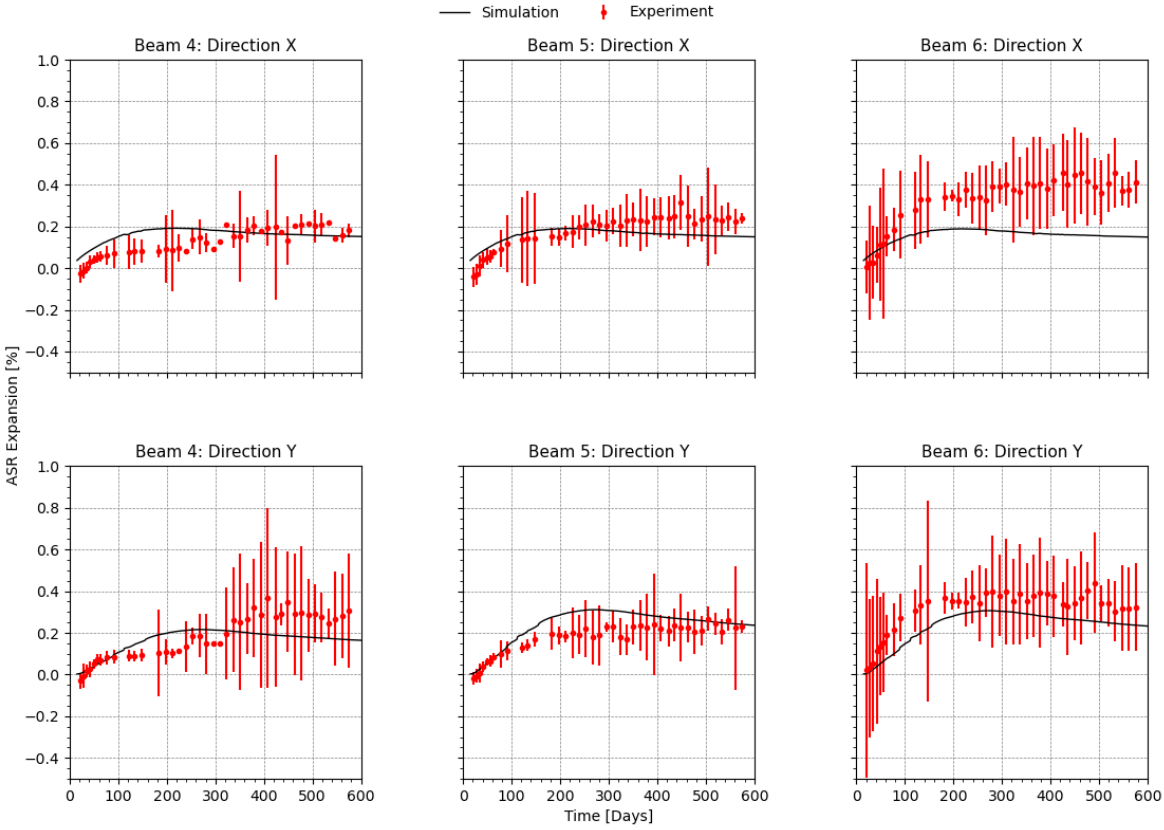


Figure 11. Comparison of the ASR expansion in $x$- and $y$-directions from experiments and Grizzly simulation.

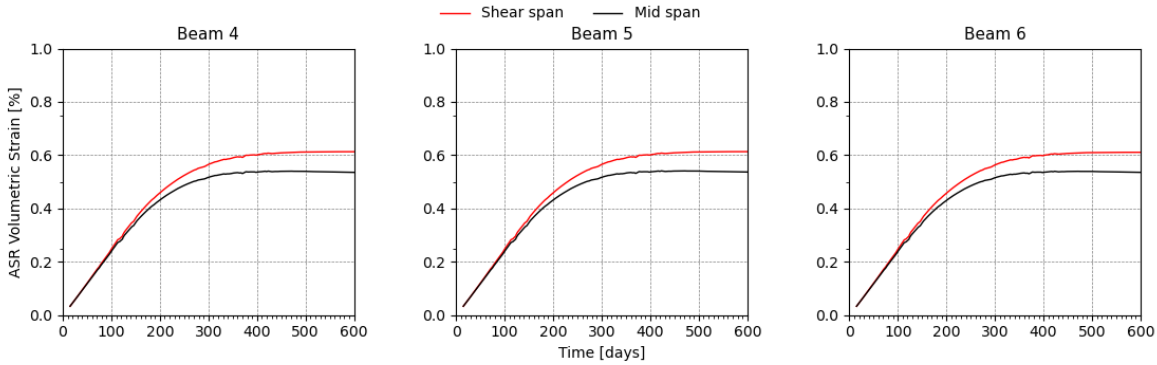


Figure 12. Comparison of the volumetric ASR expansion from experiments and Grizzly simulation.

Table 8. Modeling parameters for modeling beams in Grizzly.

| **Parameter** | **Value** |
|---|---|
| Heat transport model | Kodur-2004 |
| Aggregate type | Siliceous |
| Moisture transport model | Xi |
| Aggregate pore type | Dense |
| Cement type | U.S. Type 2 |
| Concrete cure time | 14 days |
| Aggregate volume fraction | 0.7 |
| Cement mass | 354.0 kg/m$^3$ |
| Aggregate mass | 1877.0 kg/m$^3$ |
| Water-cement ratio | 0.52 |
| Reference density of concrete | 2231.0 kg/m$^3$ |
| Reference specific heat of concrete | 1100.0 J/(Kg K) |
| Reference thermal conductivity of concrete | 3 W/(m K) |
| Reference temperature for ASR expansion | 23.0°C |
| Max volumetric expansion | 0.01125 |
| Characteristic time | 100 days |
| Latency time | 50 days |
| characteristic activation energy | 5400.0 |
| latency activation energy | 9400.0 |
| Stress latency factor | 1.0 |
| Compressive strength | 38 MPa, 37 MPa, and 34 MPa for Beam 4, Beam 5 and Beam 6, respectively |
| Compressive stress exponent | 0.0 |
| Expansion stress limit | 8.0 MPa |
| Tensile strength | 3.8 MPa, 3.7 MPa, and 3.4 MPa for Beam 4, Beam 5 and Beam 6, respectively |
| Tensile retention factor | 1.0 |
| Tensile absorption factor | 1.0 |
| Relative humidity exponent for ASR volumetric strain | 1.0 |
| Viscoelastic model | Burgers |
| Young's modulus | 27.8 GPa |
| Poisson's ratio | 0.20 |
| Concrete thermal expansion coefficient | $8.0\times10^{-6}$ 1/K |
| Steel thermal expansion coefficient | $11.3\times10^{-6}$ 1/K |
| Stress free temperature | 23.0 °C |

## 3.3 Containment Vessel Model Description

To demonstrate the ability of Grizzly to model ASR in a full structure relevant to nuclear applications, a 3D model of an idealized containment vessel was developed and simulated. Detailed information on actual nuclear power plant structures is difficult to obtain, but such information is readily available on the scale models of the containment vessels performed at Sandia National Laboratories. The 1:6 scale containment vessel structure described by Clauss [22] is used here as the basis for modeling to study ASR-induced degradation.

Rather than modeling a 1:6 scale structure, it is preferable to model a full-scale structure to appropriately consider the length scales for all physical phenomena. Thus, the dimensions of the 1:6 scale structure were scaled up to full scale in this effort. A finite element model of the considered structure is shown in Figure 13. Only half of the structure is modeled by taking advantage of symmetry. Since modeling considers angular variation in the temperature boundary conditions, the model size could not be reduced further. The modeling also considers the presence of the groundwater table and soil. Moreover, the modeling considers the effect of gravity as the compressive load may alter the ASR expansion in the structure. It should be noted that the model developed here is simplified somewhat in that it does not consider the large penetrations in the actual structure.

The material parameters used for modeling the ASR expansion while considering the thermal transport, moisture transport, creep, and presence of soil are shown in Table 9. In this research, the ASCE model [16] is used to represent the thermal conductivity and thermal capacity of concrete as it accounts for the siliceous aggregate and is applicable for normal strength concrete. Similar to thermal transport, among the multiple options for the moisture transport model, the Xi et al. [19] model is used to account for the available concrete mix parameters, such as water-cement ratio (>0.5) and cement type and curing duration.

The following assumptions are made in the modeling of the containment structure:

- The model is scaled to full scale (i.e., 1:1 scale) by keeping the same steel reinforcement ratio in the cross-sections of the structure. The same steel reinforcement ratio is obtained by altering the steel reinforcement diameter and keeping the same spacing between the steel reinforcement.

- Climate data for the air and soil are obtained from a U.S. climate station for the year 2020 [23]. Temperature and relative humidity in the air and various depth in soil for that location are shown in Figure 14.

- The basemat foundation of the containment vessel structure is resting on the soil along with a mudmat layer as a moisture barrier. The basemat of the containment vessel is assumed to be bonded to some degree with the mudmat, so glued contact is considered between basemat and mudmat of the structure.

- The non-uniform effects of sunshine and shade on the spatial distribution of the temperature are considered on the outer surface of the structure. The temperature of air and concrete in the shade is similar for most parts of the day; however, the temperature of concrete in the sunshine is observed to be approximately 16.5°C hotter than air [24]. Thus, the temperature on the angular surface of the containment vessel is assumed to be linearly increased by considering that the temperature effect from sunshine would have a maximum and minimum at $\theta = 90°$ and $\theta = -90°$, respectively. Thus, the temperature on the angular surface of a structure is estimated according to

$$T_{conc} = T_{air} + \frac{\theta + 90}{180} \Delta T_{sun-air} \tag{9}$$

  where $T_{conc}$ is concrete surface temperature, $T_{air}$ is air temperature, $\theta$ ($\in [-90°, 90°]$) is the angular coordinate of the cylindrical/dome surface of the containment vessel from a reference axis, and $\Delta T_{sun-air}$ is the difference in the temperature of the concrete surface in sun and temperature of air. The difference in the angular variation of the surface temperature temperature is shown in Figure 15.

- Since most containment vessel structures are built partially underground, the top 33% of the containment vessel structure is assumed to be above ground. Additionally, the groundwater table is assumed to be 3 m below the ground level.
- The soil is considered to be fixed at the bottom of the portion of the soil included in the model, and symmetric boundary conditions are applied on the negative $x$ face of the structure, as shown in Figure 13. Nodes along the axis of the cylinder and dome are fixed in the $y$-direction to prevent the free translation and rotation of the structure.
- Modeling also considers concrete creep using BlackBear's `GeneralizedKelvinVoigtModel`.

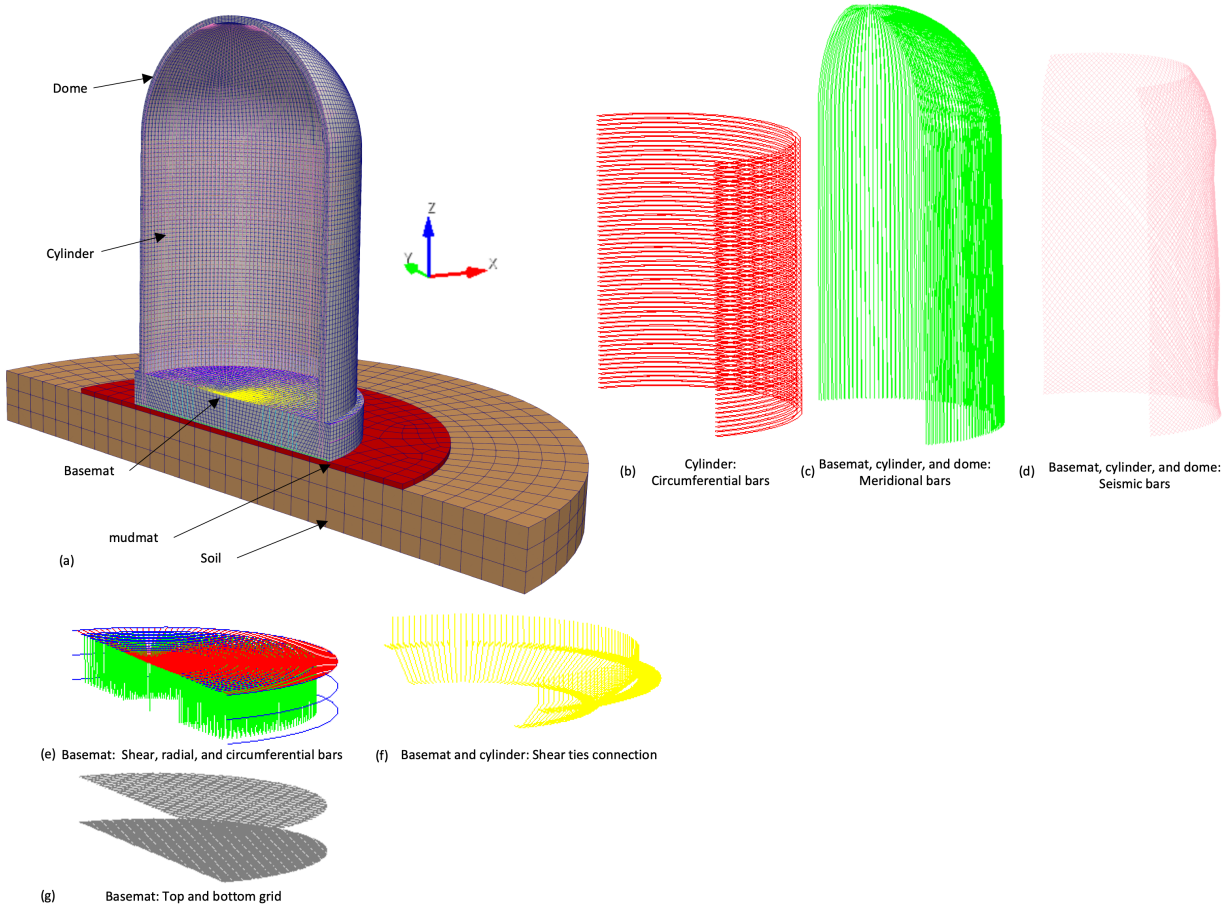


Figure 13. Axisymmetric model of a reinforced concrete containment structure to study the ASR-induced volumetric expansion: (a) two quadrants of soil, mudmat, basemat, cylindrical, and dome part of the structure with embedded (b) circumferential rebars (red) in cylindrical part of the structure, (c) meridional rebars (green) and (d) 45° inclined seismic rebars (pink) in basemat, cylindrical, and dome, (e) shear (green), radial (red), and circumferential bars (blue) in basemat, (f) shear ties (yellow) to connect basemat and cylindrical part, (g) rebars (grey) in top and bottom grid in basemat, and (h) rebars in mudmat.

Table 9. Modeling parameters used in Grizzly.

| **Parameter** | **Value** |
|---|---|
| Heat transport model | ASCE-1992 |
| Aggregate type | Siliceous |
| Moisture transport model | Xi |
| Aggregate pore type | Dense |
| Cement type | U.S. Type 2 |
| Concrete cure time | 14 days |
| Aggregate volume fraction | 0.7 |
| Cement mass | 354.0 kg/m$^3$ |
| Aggregate mass | 1877.0 kg/m$^3$ |
| Water-cement ratio | 0.53 |
| Reference density of concrete | 2231.0 kg/m$^3$ |
| Reference specific heat of concrete | 1100.0 J/(Kg K) |
| Reference thermal conductivity of concrete | 3 W/(m K) |
| Reference temperature for ASR expansion | 23.0°C |
| Max volumetric expansion | 0.01125 |
| Characteristic time | 100 days |
| Latency time | 50 days |
| characteristic activation energy | 5400.0 |
| latency activation energy | 9400.0 |
| Stress latency factor | 1.0 |
| Compressive strength | 46.9 MPa |
| Compressive stress exponent | 0.0 |
| Expansion stress limit | 8.0 MPa |
| Tensile strength | 3.45 MPa |
| Tensile retention factor | 1.0 |
| Tensile absorption factor | 1.0 |
| Relative humidity exponent for ASR volumetric strain | 1.0 |
| Viscoelastic model | Burgers |
| Young's modulus | 27.8 GPa |
| Poisson's ratio | 0.20 |
| Concrete thermal expansion coefficient | $8.0\times10^{-6}$ 1/K |
| Steel thermal expansion coefficient | $11.3\times10^{-6}$ 1/K |
| Stress free temperature | 23.0 °C |
| Soil mechanics model | Mohr Coulomb |
| Soil $\psi$ | 40° |
| Soil $\phi$ | 40° |
| Soil cohesion | 10 MPa |
| Density of soil | 2650 kg/m$^3$ |

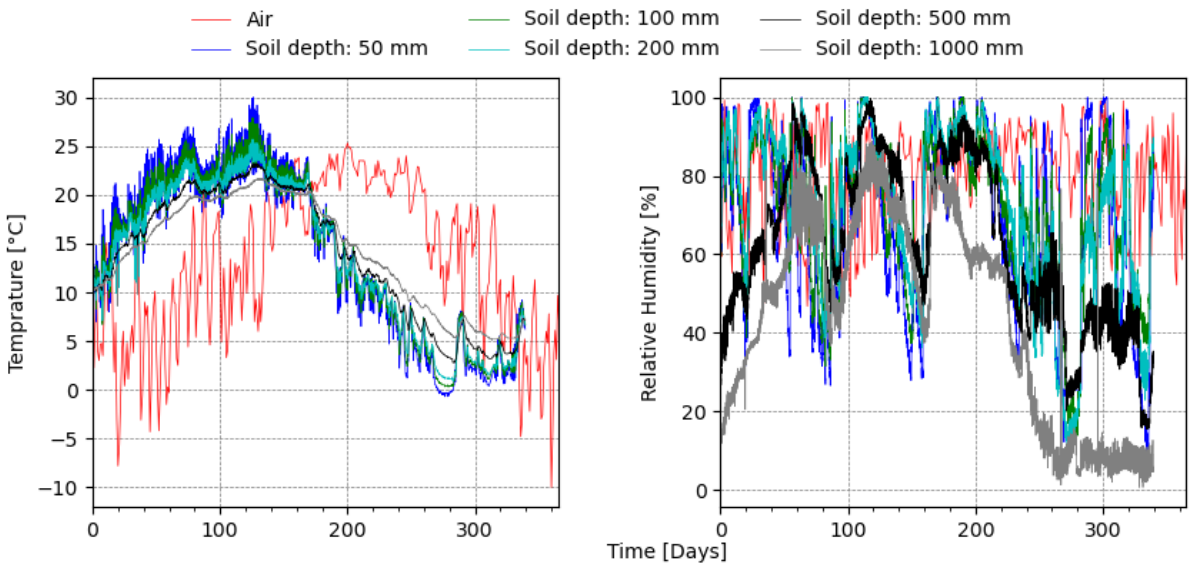


Figure 14. Temperature and relative humidity data from a U.S. climate station used in this simulation [23].

## 3.4 Containment Vessel Simulation

ASR swelling in the containment structure is measured at multiple locations on a different part of the containment vessel structure, as shown in Figure 16. Left measurement locations on each part of the structure represent exposure to a longer sunshine duration whereas right measurement locations represent a longer duration of shade. The results of the ASR swelling in radial, tangential, and vertical directions at these measurement points are shown in Figure 17. Volumetric ASR expansion, temperature, and relative humidity are also plotted for these points in the same plot. The consideration of angular variation in temperature affects the ASR expansion in all directions. Furthermore, the volumetric ASR expansion in the longer sunshine region is observed more as compared to the longer shade region. Volumetric expansion is observed to be the same throughout the height of the structure, which is due to the higher relative humidity and lower temperature in the underground part of the structure as compared to the aboveground part of the structure.

Because the conditions at an actual nuclear power plant will invariably differ from those modeled here, this simulation is primarily useful as a proof of concept. It demonstrates that Grizzly is able to model coupled moisture transport, heat transfer, and mechanical deformation, including the effects of ASR. This is all done on a large model that includes a complex rebar arrangement. This problem has been added to Grizzly's assessment test suite for use as an example problem, and these capabilities could readily be applied to other structures of interest.

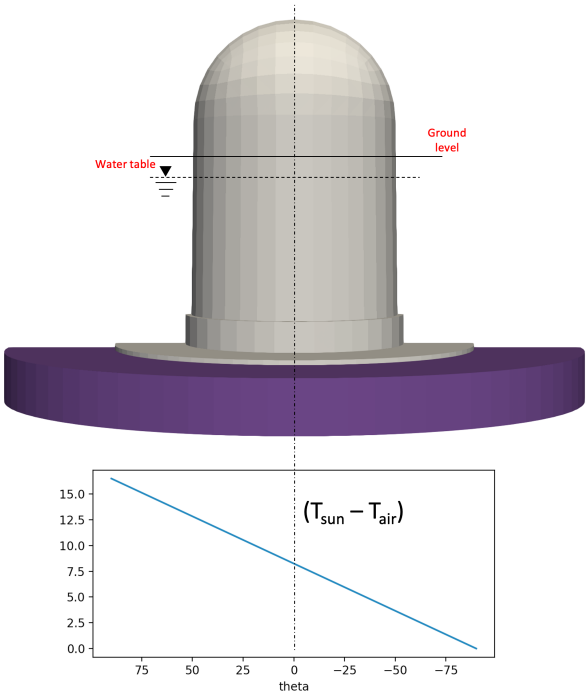


Figure 15. Angular variation in temperature difference between surface exposed to sunshine and air.

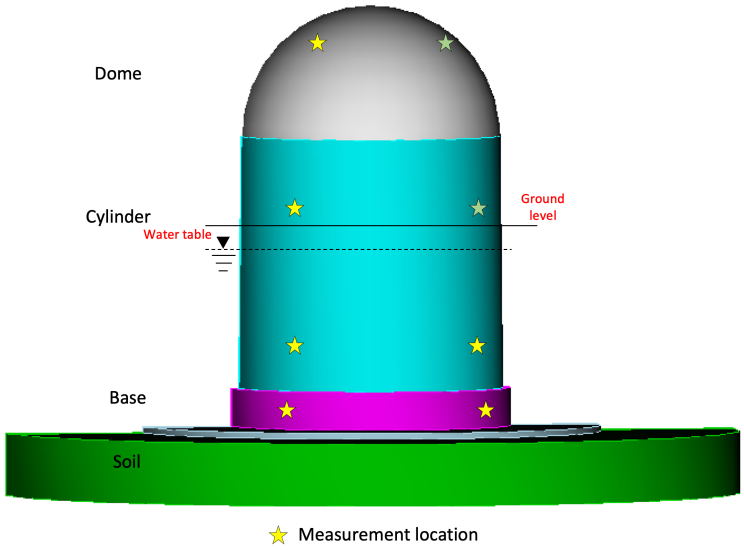


Figure 16. Measurement location on the dome, cylinder, and base part of the containment vessel structure.

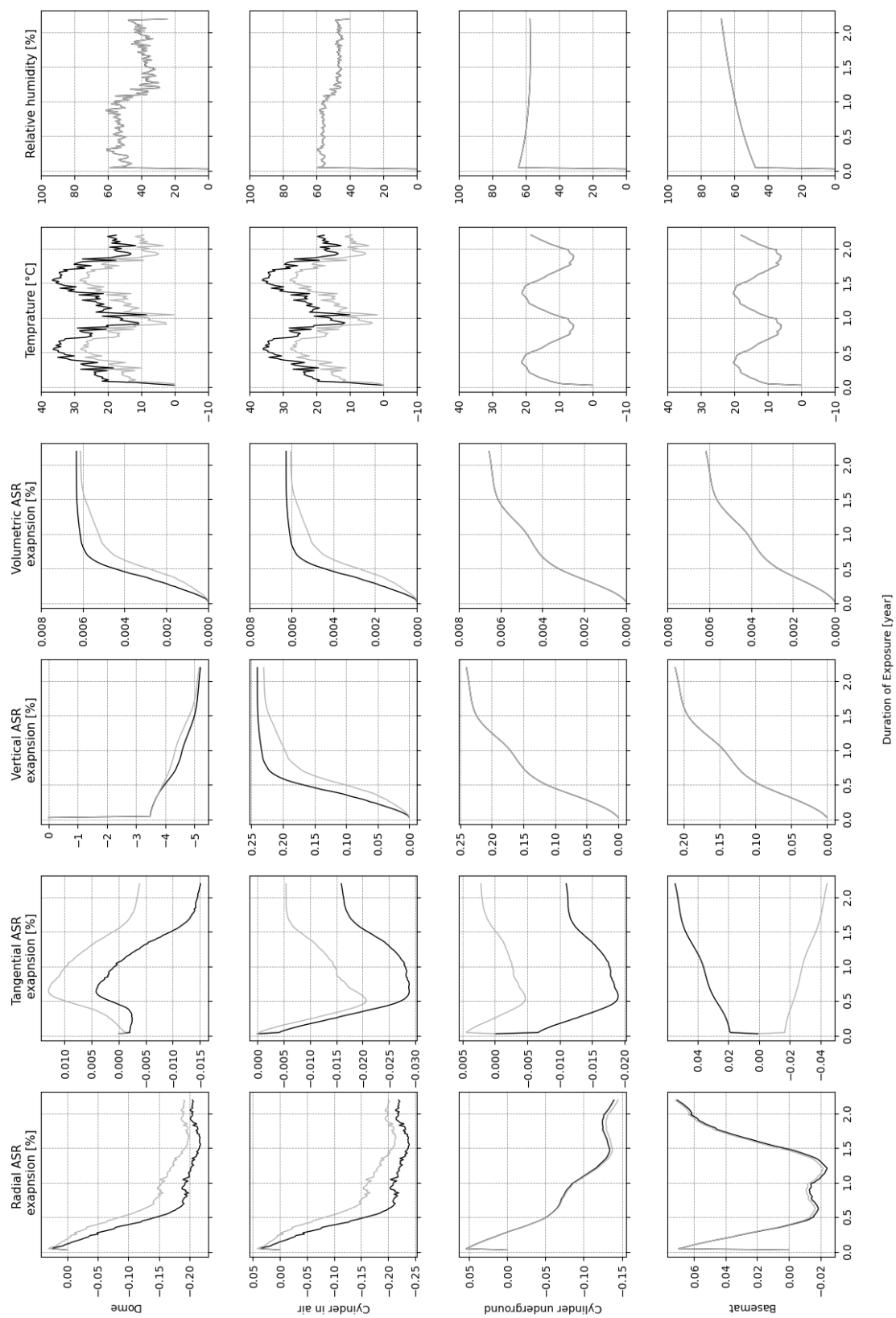


Figure 17. ASR expansion in radial, tangential, and vertical directions; volumetric ASR expansion; temperature; and relative humidity in dome, cylinder (in air), cylinder (underground), and basemat part of the containment vessel structure.

# 4 Release of the Grizzly and BlackBear Codes

One of the objectives of the present work was to provide an updated release of the Grizzly code. In the past, two versions of Grizzly have been issued: Version 1.0 [25] and Version 2.0 [26], corresponding to the addition of significant features for the Light Water Reactor Sustainability (LWRS) program. These releases were made by creating tags on the Grizzly git repository used to manage the source code.

In recent years, there has been a significant effort to ensure that the development of the Multiphysics Object-Oriented Simulation Environment (MOOSE) framework and some of the applications that are based on it to comply with the ASME NQA-1 standards for software quality. As part of that effort, the systems for documentation, testing, and generation of software quality-related documents have been standardized. Now a web-based system for documentation is used, and that documentation is generated from a combination of information in the software source code, as well as supporting information provided in separate files in the source code repository. A standardized system is now used for the naming of code releases, in which the code releases are based on the date of their release.

Because portions of Grizzly's capabilities are provided by the BlackBear code, as well as the MOOSE framework, a release of Grizzly also requires a release of BlackBear and MOOSE. In 2021, two releases of these sets of code were made. The first was the 2021-05-18 release, which was made prior to an assessment of these codes by independent auditors on its compliance with NQA-1 processes. The second release is the 2021-09-15 release, which includes recent updates to the fracture mechanics and concrete models necessary to model the problems shown here. In addition, this version of Grizzly includes the containment vessel test case described in this report.

The full set of documentation for the released code is provided in the form of a set of web pages. The documentation for the latest release of the BlackBear code, which is openly available, is hosted at `https://mooseframework.inl.gov/releases/blackbear/2021-09-15/`. The Grizzly documentation is hosted on an internal INL server that users with access to Grizzly have access to. Users with access to the code can also build that set of websites for hosting on their own system.

# 5 Summary and Future Work

Development and testing of Grizzly in two important areas were performed in this effort. For RPVs, a more accurate set of reduced-order fracture mechanics models that eliminates excess conservatisms was tested and incorporated into its models used for PFM calculations. Direct evaluations of detailed 3D models over a significant portion of the parameter space were performed and generally showed good agreement with the ROMs. There were some discrepancies in the higher order terms in some cases that need further investigation. Preliminary evaluations indicate that these updated models result in significantly decreased probabilities of crack initiation.

There are multiple areas for further work in this fracture modeling. The aforementioned issues with the accuracy of the models in some regimes need further investigation. These are not expected to result in significant changes in the solutions because they only affect higher order terms, but should be investigated nonetheless. The regions of applicability of the ROMs should be further expanded to include the full parameter space. Currently, a small percentage of the flaws are not covered by these models, but those flaws are expected to be significant contributors to the PFM results. Finally, a more extensive evaluation of the effects of using these updated models on full RPV models is warranted.

In the area of concrete modeling, ASR-induced degradation in reinforced concrete structures was validated using reinforced concrete beams and demonstrated on a nuclear containment vessel structure. The ASR expansion is dependent on the temperature, moisture, confinement, and state of stress. This effort has shown how the models reasonably predict the response of the laboratory specimens and are able to model a large reinforced concrete structure with complex rebar configurations. This has demonstrated that Grizzly has a robust capability for this type of modeling. The main areas for future work here are in further testing to ensure robustness under a wide variety of conditions, as well as more validation against experimental data. It is also important to note that this effort only considered ASR. Grizzly also has models for RIVE, and there are similar validation and testing needs for that capability. Finally, there are other important degradation mechanisms for which models have not yet been implemented in Grizzly, but which would readily fit within this framework.

# 6 Acknowledgments

This work was funded by the U.S. Department of Energy Office of Nuclear Energy's Light Water Reactor Sustainability (LWRS) programs. This manuscript has been authored by a contractor of the U.S. Government under Contract DE-AC07-05ID14517. Accordingly, the U.S. Government retains a non-exclusive, royalty free license to publish or reproduce the published form of this contribution, or allow others to do so, for U.S. Government purposes.

This research made use of the resources of the High Performance Computing Center at Idaho National Laboratory, which is supported by the Office of Nuclear Energy of the U.S. Department of Energy and the Nuclear Science User Facilities under Contract No. DE-AC07-05ID14517.

# 7 References


[1] K. Lu, M. Akihiro, J. Katsuyama, Y. Li, and F. Iwamatsu. "Development of Stress Intensity Factors for Subsurface Flaws in Plates Subjected to Polynomial Stress Distributions". In: *Journal of Pressure Vessel Technology* 140.3 (2018). 031201.

[2] B. Spencer, W. Hoffman, and M. Backman. "Modular system for probabilistic fracture mechanics analysis of embrittled reactor pressure vessels in the Grizzly code". In: *Nuclear Engineering and Design* 341 (Jan. 2019), pp. 25–37.

[3] P. Williams, T. Dickson, B. R. Bass, and H. B. Klasky. *Fracture Analysis of Vessels – Oak Ridge, FAVOR, v16.1, Computer Code: Theory and Implementation of Algorithms, Methods, and Correlations*. Tech. rep. ORNL/LTR-2016/309. Oak Ridge, TN: Oak Ridge National Laboratory, Sept. 2016.

[4] *ASME Boiler and Pressure Vessel Code, Section XI, Rules for Inspection and Testing of Nuclear Power Plant Components, Division 1, Rules for Inspection and Testing of Components of Light-Water-Cooled Plants*. ASME BPVC.XI.1-2021. ASME, 2021.

[5] H. F. Bückner. "A novel principle for the computation of stress intensity factors". In: *Z. angew Math. Mech.* 50 (1970), pp. 529–546.

[6] R. C. Cipolla. *Computational Method to Perform the Flaw Evaluation Procedure as Specified in the ASME Code, Section XI, Appendix A*. Tech. rep. EPRI Report NP-1181. Failure Analysis Associates, Sept. 1979.

[7] B. W. Spencer, W. M. Hoffman, and W. Jiang. *Enhancements to Engineering-scale Reactor Pressure Vessel Fracture Capabilities in Grizzly*. Tech. rep. INL/EXT-17-43427. Idaho National Laboratory, Sept. 2017.

[8] T. Belytschko and T. Black. "Elastic crack growth in finite elements with minimal remeshing". In: *International Journal for Numerical Methods in Engineering* 45.5 (June 1999), pp. 601–620.

[9] T. Nakamura and D. M. Parks. "Determination of elastic T-stress along three-dimensional crack fronts using an interaction integral". In: *International Journal of Solids and Structures* 29.13 (1992), pp. 1597–1611.

[10] M. C. Walters, G. H. Paulino, and R. H. Dodds. "Interaction integral procedures for 3-D curved cracks including surface tractions". In: *Engineering Fracture Mechanics* 72.11 (July 2005), pp. 1635–1663.

[11] R. T. T. Hastie and J. Friedman. *The Elements of Statistical Learning*. Springer, 2001.

[12] B. W. Spencer, W. M. Hoffman, S. Biswas, and A. Jain. *Assessment of Grizzly Capabilities for Reactor Pressure Vessels and Reinforced Concrete Structures*. Tech. rep. INL/EXT-20-59941. Idaho National Laboratory, Sept. 2020.

[13] W. M. Hoffman and B. W. Spencer. *Benchmarking of Probabilistic Fracture Mechanics Models in Grizzly*. Tech. rep. INL/EXT-21-62199. Idaho National Laboratory, 2021.

[14] V. Saouma and L. Perotti. "Constitutive Model for Alkali-Aggregate Reactions". en. In: *ACI Materials Journal* 103.3 (2006).

[15] V. Kodur, T. Wang, and F. Cheng. "Predicting the fire resistance behaviour of high strength concrete columns". In: *Cement and Concrete Composites* 26.2 (2004), pp. 141–153.

[16] ASCE. *Structural Fire Protection, ASCE Committee on Fire Protection, Structural Division*. Tech. rep. New York, NY: American Society of Civil Engineers, 1992.

[17] Eurocode. *Design of concrete structures. Part 1-2: general rules - structural fire design*. Tech. rep. European Committee for Standardization, Brussels, Belgium., 2004.

[18] Z. P. Bažant, J.-C. Chern, and W. Thonguthai. “Finite element program for moisture and heat transfer in heated concrete”. In: *Nuclear Engineering and Design* 68.1 (1982), pp. 61–70.

[19] Y. Xi, Z. P. Bažant, L. Molina, and H. M. Jennings. “Moisture diffusion in cementitious materials Moisture capacity and diffusivity”. en. In: *Advanced Cement Based Materials* 1.6 (Nov. 1994), pp. 258–266.

[20] R. Mensi, P. Acker, and A. Attolou. “Séchage du béton: analyse et modélisation”. In: *Materials and structures* 21.1 (1988), pp. 3–12.

[21] R. Ballarini, B. Gencturk, A. Jain, H. Aryan, Y. Xi, M. Abdelrahman, and B. Spencer. *Multiple Degradation Mechanisms in Reinforced Concrete Structures, Modeling and Risk Analysis*. Tech. rep. INL/EXT-20-57095. Idaho National Laboratory, Feb. 2020.

[22] D. B. Clauss. *Round-Robin Pretest Analyses of a 1:6-Scale Reinforced Concrete Containment Model Subject to Static Internal Pressurization*. Tech. rep. NUREG/CR-4913, SAND87-0891. Albuquerque, NM: Sandia National Laboratories, May 1987.

[23] J. E. Bell, M. A. Palecki, C. B. Baker, W. G. Collins, J. H. Lawrimore, R. D. Leeper, M. E. Hall, J. Kochendorfer, T. P. Meyers, T. Wilson, and H. J. Diamond. “U.S. Climate Reference Network Soil Moisture and Temperature Observations”. In: *Journal of Hydrometeorology* 14.3 (2013), pp. 977–988.

[24] D. Armson, P. Stringer, and A. Ennos. “The effect of tree shade and grass on surface and globe temperatures in an urban area”. In: *Urban Forestry & Urban Greening* 11.3 (2012), pp. 245–255.

[25] B. W. Spencer. “Grizzly Beta 1.0 Release”. In: *LWRS Newsletter* 23 (2017), pp. 10–11.

[26] B. W. Spencer and T. Hu. *Enhancements to Concrete Modeling Capabilities in Grizzly 2.0*. Tech. rep. INL/EXT-18-51526. Idaho National Laboratory, Sept. 2018.